The Astrophysical Journal, 734:33 (20pp), 2011 June 10 doi:10.1088/0004-637X/734/1/33

INVESTIGATING THE NUCLEAR ACTIVITY OF BARRED SPIRAL GALAXIES: THE CASE OF NGC 1672

L. P. Jenkins[1,2], W. N. Brandt[3,4], E. J. M. Colbert[2], B. Koribalski[5], K. D. Kuntz[2], A. J. Levan[6], R. Ojha[7], T. P. Roberts[8], M. J. Ward[8], and A. Zezas[9]
[1] Laboratory for X-ray Astrophysics, NASA Goddard Space Flight Center, Code 662, Greenbelt, MD 20771, USA
[2] Johns Hopkins University, Baltimore, MD 21218, USA
[3] Department of Astronomy & Astrophysics, The Pennsylvania State University, University Park, PA 16802, USA
[4] Institute for Gravitation and the Cosmos, The Pennsylvania State University, University Park, PA 16802, USA
[5] CSIRO, Australia Telescope National Facility (ATNF), Epping, NSW 1710, Australia
[6] Department of Physics, University of Warwick, Coventry CV4 7AL, UK
[7] NVI/United States Naval Observatory, Washington, DC 20392, USA
[8] Department of Physics, Durham University, Durham DH1 3LE, UK
[9] Department of Physics, University of Crete, GR-71003 Heraklion, Greece
Received 2009 June 10; accepted 2011 January 12; published 2011 May 24

ABSTRACT

We have performed an X-ray study of the nearby barred spiral galaxy NGC 1672, primarily to ascertain the effect of the bar on its nuclear activity. We use both *Chandra* and *XMM-Newton* observations to investigate its X-ray properties, together with supporting high-resolution optical imaging data from the *Hubble Space Telescope* (*HST*), infrared imaging from the *Spitzer Space Telescope*, and Australia Telescope Compact Array ground-based radio data. We detect 28 X-ray sources within the D_{25} area of the galaxy; many are spatially correlated with star formation in the bar and spiral arms, and two are identified as background galaxies in the *HST* images. Nine of the X-ray sources are ultraluminous X-ray sources, with the three brightest ($L_X > 5 \times 10^{39}$ erg s^{-1}) located at the ends of the bar. With the spatial resolution of *Chandra*, we are able to show for the first time that NGC 1672 possesses a hard ($\Gamma \sim 1.5$) nuclear X-ray source with a 2–10 keV luminosity of 4×10^{38} erg s^{-1}. This is surrounded by an X-ray-bright circumnuclear star-forming ring, comprised of point sources and hot gas, which dominates the 2–10 keV emission in the central region of the galaxy. The spatially resolved multiwavelength photometry indicates that the nuclear source is a low-luminosity active galactic nucleus (LLAGN), but with star formation activity close to the central black hole. A high-resolution multiwavelength survey is required to fully assess the impact of both large-scale bars and smaller-scale phenomena such as nuclear bars, rings, and nuclear spirals on the fueling of LLAGN.

Key words: galaxies: evolution – galaxies: individual (NGC 1672) – galaxies: nuclei – galaxies: spiral

Online-only material: color figures

1. INTRODUCTION

The presence of a bar in a galaxy plays an important role in its evolution. Approximately two-thirds of all spiral galaxies are barred (e.g., Eskridge et al. 2000; Menéndez-Delmestre et al. 2007), so any complete picture of galaxies must include the impact of bars on both their nuclear and extranuclear properties. Secular (i.e., internal) galaxy evolution involving bars, oval distortions, and spiral structure can have a significant effect when a galaxy is no longer merging or interacting strongly with other galaxies (see Kormendy & Kennicutt 2004). For example, there is believed to be a causal connection between the existence of a bar and a galaxy's circumnuclear properties. Bars can drive gas from the outer disk to the inner regions of the galaxy; gas clouds are shocked as they encounter the leading edge of the bar, lose angular momentum, and flow toward the galaxy's center (Shlosman et al. 1990). An observable result of this is that a substantial fraction of galaxies with bars show enhanced star formation activity in their central regions, and the inflow of material is also believed to build "pseudobulges," which are distinct from classical galaxy bulges (Kormendy & Kennicutt 2004). A strong global density pattern such as a bar can also produce a series of resonances between the angular velocity of the bar and the orbital motions of stars and gas in the disk, where rings can form (Buta 1999). Indeed, some galaxies with bars are known to have circumnuclear rings of star formation (e.g., Buta & Combes 1996; Knapen 2005a), resulting from increased gas density at or near the inner Lindblad resonance (ILR).

A question that we are addressing with this study is can the material driven to the center of a galaxy by the bar also fuel an active galactic nucleus (AGN)? While there is clear observational evidence that bars in disk galaxies cause higher central concentrations of gas (and hence centrally concentrated star formation) compared to non-barred galaxies, it is unclear whether a large-scale bar is sufficient to transport material close enough for AGN feeding (typically on AU scales; see Knapen 2005b for a review). Additionally, in an X-ray study by Maiolino et al. (1999) using *Ginga*, *ASCA*, and *BeppoSAX* data, a strong correlation was found between absorbing column density toward Type-2 Seyfert nuclei and the presence of a strong bar, i.e., more than 80% of Compton-thick Seyfert 2s are barred. This suggests that if a low-luminosity AGN (LLAGN) is present, it may be obscured from view at optical wavelengths and/or diluted by strong star formation activity, which could lead to a misclassification as a pure star-forming nucleus.

The topic of the influence of bars on galaxy evolution is not well studied at X-ray energies, but we are now able to utilize the excellent complementary imaging and spectral capabilities of *Chandra* and *XMM-Newton* to make detailed investigations of the X-ray characteristics of these systems. In particular, high-spatial-resolution X-ray observations with *Chandra* provide an ideal method for searching for low-level AGN activity in nearby

galaxies, in the form of a hard central point source that may not be visible at other wavelengths. It also allows us to separate potential AGN activity from other types of X-ray sources that may reside close to the nucleus, such as X-ray binaries (XRBs) associated with circumnuclear star formation. Indeed, X-ray surveys utilizing *Chandra* have proved successful in recent years in identifying previously unknown LLAGN activity in nearby galaxies. In particular, X-ray nuclei spanning a wide range of X-ray luminosities ($\sim 10^{37}$–10^{44} erg s^{-1}, 2–10 keV) have been detected in a large fraction (typically ∼45%–70%) of galaxies hosting low-ionization nuclear emission regions (LINERs; Heckman 1980) as well as galaxies classed as having H II or transition nuclei (e.g., Ho et al. 2001; Terashima & Wilson 2003; Satyapal et al. 2004, 2005; Dudik et al. 2005; Flohic et al. 2006; González-Martín et al. 2006, 2009; Zhang et al. 2009; Desroches & Ho 2009). Studies at other wavelengths have also recently been used to uncover previously unknown AGN activity in nearby galaxies. For example, *Spitzer* infrared (IR) spectroscopic surveys have revealed bona fide AGN in both LINERs and IR-bright galaxies, some of which showed no sign of such activity in optical studies (Dudik et al. 2009; Goulding & Alexander 2009). High-resolution radio imaging has been shown to be an efficient method for finding LLAGN activity; compact radio nuclei have been found in $\gtrsim$50% of LINERs/LLAGNs, which are thought to be attributable to relativistic jets produced by accreting supermassive black holes (Nagar et al. 2005, and references therein).

To begin to address the nature of the nuclear (and off-nuclear) X-ray emission in barred galaxies, we have conducted a pilot study of the barred galaxy NGC 1672, using X-ray observations from both *Chandra* (40 ks) and *XMM-Newton* (50 ks). Here, we report the results from these observations and use supporting *Hubble Space Telescope*/Advanced Camera for Surveys (*HST*/ACS), *Spitzer,* and Australia Telescope Compact Array (ATCA) radio observations to assist in the interpretation of the X-ray results. This paper is laid out as follows. In Section 2, we give background information on the target galaxy NGC 1672. In Section 3, we describe the *Chandra*, *XMM-Newton*, *HST*/ACS, *Spitzer,* and ATCA radio observations and data analysis techniques, and in Section 4 we present our results. In Section 5 we discuss the nature of the nuclear emission, and in Section 6 we compare our results with those for other barred and non-barred galaxies in the literature. Throughout this paper, we use a distance to NGC 1672 of 16.3 Mpc, corresponding to a recession velocity of 1140 km s^{-1} relative to the centroid of the Local Group (Osmer et al. 1974), with $H_0 = 70$ km s^{-1} Mpc^{-1}.

2. NGC 1672

For this pilot study, we have selected the nearby (16.3 Mpc) late-type barred spiral galaxy NGC 1672 (SB(r)bc). It has a moderately low inclination angle ($i = 34°$; de Vaucouleurs et al. 1991) and is known to have a strong bar (2.′4 in length, corresponding to 11.4 kpc at a distance of 16.3 Mpc), many H II regions in its four spiral arms, plus vigorous star formation at the ends of the bar (Brandt et al. 1996, and references therein). It has a high IR luminosity ($\log L_{\rm FIR}/L_{\odot} = 10.2$) and a global star formation rate (SFR) of 2.7 $M_{\odot}$ yr^{-1} (Kewley et al. 2000).

Optical studies have given conflicting evidence as to the nature of the nuclear activity in NGC 1672. It was noted by Sérsic & Pastoriza (1965) as having a complex or "amorphous" nuclear morphology, and was subsequently shown by Storchi-Bergmann et al. (1996) to possess a circumnuclear ring of star formation, measuring ∼11″ × 9″ (0.9 × 0.7 kpc at a distance of 16.3 Mpc), located between two ILRs. Therefore, studies of its nuclear properties that use large apertures are strongly affected by the star formation in the ring. For example, Osmer et al. (1974) showed that the optical emission spectrum in the central 17″ was similar to those of normal H II nuclei, but with an Hα/Hβ ratio indicative of a large amount of dust reddening. Storchi-Bergmann et al. (1995) also measured optical emission-line ratios in a relatively large 10″ × 20″ aperture, and classified the nucleus as "composite," with ratios between those of typical starburst and Seyfert values. More recent optical line ratio diagnostics by Kewley et al. (2000) of the emission within a ∼13″ slit are indicative of an H II-type nucleus, with no Hα line broadening detected. All of these studies will have been strongly contaminated by the emission from the circumnuclear starburst ring; however, they do demonstrate that this component is dominant, and that any potential AGN activity would be relatively weak.

More detailed, spatially resolved studies have also given ambiguous results. Veron et al. (1981) detected possible broadening of [O III] (∼300 km s^{-1}) compared to Hβ lines (∼150 km s^{-1}) in the central 2″ × 4″, which they suggested was evidence of a composite H II/Seyfert 2 nucleus. Garcia-Vargas et al. (1990) performed a high-spatial-resolution spectral analysis of the nucleus, and found a strong increase in the [O III]/Hβ ratio in the central 1″ compared to its immediate surroundings. However, both lines had the same FWHM of ∼300 km s^{-1}, and the authors classified the nucleus as a LINER. Storchi-Bergmann et al. (1996) also measured spatially resolved (2″) emission-line ratios, which were better modeled by a LINER-type stellar photoionization model with $T_{\rm eff} \geqslant 45{,}000$ K, rather than photoionization by a strong AGN continuum.

NGC 1672 has previously been observed with at X-ray wavelengths with *ROSAT* and *ASCA*. Three bright X-ray sources were detected in the soft 0.2–2 keV band with the *ROSAT*/HRI and PSPC, which were clearly associated with the galaxy (Brandt et al. 1996; de Naray et al. 2000). The brightest source was located at the nucleus, while the other two were co-spatial with the ends of the bar. The nucleus had a soft X-ray spectrum consistent with thermal emission with a temperature of 0.68 keV, and a soft X-ray luminosity of 7×10^{39} erg s^{-1} (0.2–2 keV). However, these studies were again unable to resolve the nuclear emission spatially due to the 5″ FWHM of the HRI point-spread function (PSF), and so could not determine whether the bulk of the soft emission came from a starburst or AGN. Furthermore, the *ASCA* data showed no evidence of significant hard (2–10 keV) emission from the nuclear source, with the hard emission in the galaxy being dominated by two off-nuclear X-ray sources (X-3 and X-7, see Figure 4(b) in de Naray et al. 2000). Thus, it was concluded that if an active nucleus is present in NGC 1672, it must be Compton-thick, with $N_{\rm H} > 2 \times 10^{24}$ cm^{-2}.

3. OBSERVATIONS AND DATA REDUCTION

3.1. Chandra Observations

NGC 1672 was observed with *Chandra* for 40 ks on 2006 April 30 (ObsID 5932) using the back-illuminated S3 chip of the Advanced CCD Imaging Spectrometer (ACIS). The field of view (FOV) of the observation is shown in Figure 1; the nucleus of the galaxy was placed at the aimpoint of the S3 chip, and the observation encompasses the entire D_{25}[10] extent of the

[10] D_{25} = the apparent major isophotal diameter measured at the surface brightness level $\mu_{\rm B} = 25.0$ mag arcsec^{-2}.

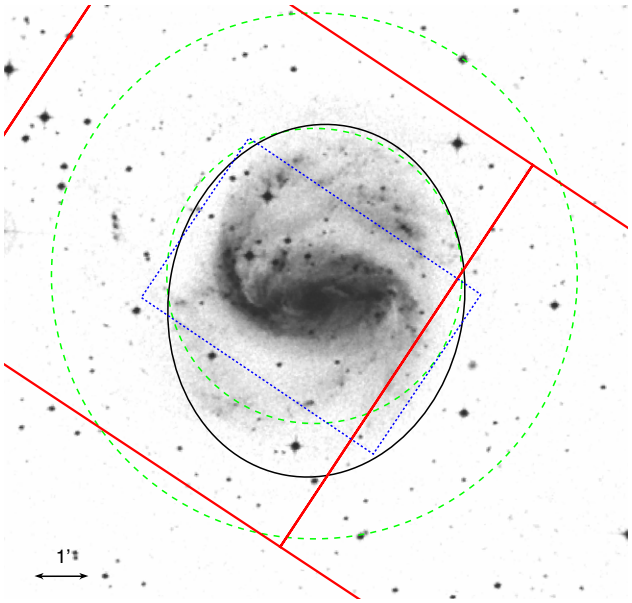

Figure 1. DSS optical image of NGC1672 showing the *Chandra* ACIS-S field of view (solid red), the *HST*/ACS field of view (dotted blue), and the 3 and 6 cm radio beam sizes (dashed green circles of 5.″5 and 9.″8 diameters, respectively). The D_{25} ellipse of the galaxy is shown with a solid (black) line. The *XMM-Newton* and *Spitzer* observations cover the D_{25} area of the galaxy. North is up and east is to the left.

(A color version of this figure is available in the online journal.)

galaxy. The data were initially processed with the *Chandra* Interactive Analysis of Observations (CIAO) tool suite version 3.3, with CALDB version 3.2.1. The processing included a charge transfer efficiency correction and time-dependent gain correction. Further data analysis was performed using CIAO version 3.4. A full-field light curve was extracted from the level-2 event list to search for periods of high background, but no strong flares were found, leaving a net exposure time of 39.6 ks.

3.1.1. Imaging and Source Detection

The basic data reduction was done using standard CIAO data analysis threads.[11] Images were created of an $8' \times 8'$ region (encompassing the full D_{25} area of the galaxy) at full 0.″492 pixel resolution in soft (0.3–1 keV), medium (1–2 keV), hard (2–10 keV), and broad (0.3–10 keV) energy bands. Monochromatic exposure maps were created at 0.8, 1.0, and 2.0 keV, corresponding to the peak energy in the soft, medium, and hard-band data. The images were adaptively smoothed using the `csmooth` task, with a fairly low significance of 2σ above the local background (corresponding to ∼1–30 pixels in the body of the galaxy) to avoid oversmoothing of faint features in the central region (see Section 4.3).

Initial detection of candidate sources was carried out in each energy-band image using the CIAO task `wavdetect`, a Mexican Hat wavelet source detection algorithm. Wavelet scales of 1.0, 1.414, 2.0, 2.828, 4.0, 5.657, and 8.0 pixels were used, and the significance threshold was set to 1.0×10^{-6} corresponding to approximately one false detection per band over the $8 \times 8'$ field. A merged source list was created that included sources detected in all bands, which was used as the input list for source parameterization in the `ACIS Extract`[12] IDL software (AE; Broos et al. 2010). The main steps in the procedure are (1) the definition of source extraction regions based on the 90% contour of the local PSF, (2) trial extraction of events within those regions, (3) improvement of positions if necessary (see below), and (4) full extraction of source and background spectra using final positions, and the creation of associated response matrix files (RMFs) and ancillary response files (ARFs) for each source.

Source positions were improved (in step 3) using the `CHECK_POSITIONS` stage, which computes "mean data" and "correlation" positions for all sources. The "mean data" position corresponds to the central position of the extracted in-band events in the 0.3–10 keV band, while the "correlation" positions are obtained by convolving the data image with a position-dependent model PSF. The offsets between these and the original `wavdetect` positions were typically 0.1–0.″8. The position estimates were visually reviewed, and the best was chosen for each source. Where there was little difference between the estimates, the original position was retained.

The source extraction regions were based on the 90% contour of the local PSF at the final positions. Background spectra were extracted in local annuli, with inner radii of 1.1 times the 99% radius of the PSF (to exclude any residual source flux), and outer radii tailored so that each background spectrum contained at least 100 counts. For the central (ring) region, the whole area (17″ radius) was masked out from the background map due to the clumpy diffuse emission in the area, and the background subtraction for sources in this region (except for the nucleus) was performed using the area immediately outside this.

Due to the complexity of the central region, the spectrum of the nuclear X-ray source was extracted manually in CIAO using `specextract`. The source aperture was set to 1.″2 radius, centered on the position from `wavdetect` ($04^{h}45^{m}42\overset{s}{.}5$, $-59°14'50\overset{''}{.}1$). The local background flux was measured in an annulus immediately outside this (1.″2–2.″0 radius), and was chosen using the radio contours as a guide in order to cover as much of the area inside the ring, without encountering any ring emission (see Section 4.3). Any other typical non-local background region would have left residual soft emission in the nuclear source counts.

Since there is significant diffuse emission in the circumnuclear ring area, it is possible that some of the candidate sources detected there may be clumpy gas rather than true point sources. To test this, we performed PSF fitting using the AE task `AE_RADIAL_PROFILE`, which computes a one-sided Kolmogorov-Smirnov (K-S) probability to determine whether the observed counts in the 1–2 keV energy range are consistent with the model local 1.49 keV PSF encircled energy distribution. Six candidate sources in the ring region were inconsistent with the local PSF profile with a significance of >99%. Sources without detections in the hard 2–10 keV band and with a K-S probability >99% were deemed to be diffuse and discarded.

The final *Chandra* catalog contains 28 sources inside the D_{25} ellipse, and their properties are listed in Table 1. Sources with significance of $>2.5\sigma$ were retained, including faint *Chandra* counterparts to two significantly detected *XMM-Newton* sources (for variability and completeness). This detection threshold corresponds to >12 net source counts. Source fluxes were determined using spectral fitting (see Section 3.3).

The absolute astrometry of *Chandra* is generally accurate to within ∼1″.[13] To confirm this, the X-ray positions were compared to the Two Micron All Sky Survey (2MASS) point

[11] http://asc.harvard.edu/ciao/threads/index.html
[12] http://www.astro.psu.edu/xray/docs/TARA/ae_users_guide.html
[13] http://cxc.harvard.edu/cal/ASPECT/celmon/

Table 1
NGC 1672 X-ray Source Properties

Src	J2000	*XMM-Newton* (2004 November)						*Chandra* (2006 April)					
		cts s^{-1} ($\times 10^{-3}$) M1/M2/PN	N_H[a]	Γ	χ^2/dof	F_X[b]	L_X[c]	cts s^{-1} ($\times 10^{-3}$)	N_H[a]	Γ	χ^2/dof	F_X[b]	L_X[c]
1	044528.47−591433.4	1.85/1.44/4.89	<1.02	$1.25^{+0.23}_{-0.16}$	15.80/13	$3.98^{+0.24}_{-0.47}$	$1.27^{+0.08}_{-0.15}$	2.63	$6.61^{+5.60}_{-3.70}$	$2.17^{+1.20}_{-1.11}$	1.26/1	$2.29^{+0.43}_{-0.65}$	$0.73^{+0.14}_{-0.21}$
2	044529.80−591328.7	0.38/0.37/1.36	...	...	...	$0.73^{+0.20}_{-0.17}$	$0.23^{+0.07}_{-0.05}$	1.04	...	...	...	$0.93^{+0.28}_{-0.24}$	$0.29^{+0.09}_{-0.08}$
3	044529.84−591506.9	0.83/0.67/1.90	...	...	...	$1.22^{+0.12}_{-0.17}$	$0.39^{+0.04}_{-0.05}$	1.49	...	...	...	$1.28^{+0.35}_{-0.27}$	$0.41^{+0.11}_{-0.09}$
4	044531.61−591454.6	2.82/2.70/12.56	$1.51^{+0.57}_{-0.45}$	$2.42^{+0.20}_{-0.22}$	27.95/34	$4.13^{+0.24}_{-0.33}$	$1.31^{+0.08}_{-0.11}$	23.28	$1.67^{+0.53}_{-0.47}$	$1.75^{+0.19}_{-0.17}$	35.71/36	$21.74^{+1.60}_{-2.51}$	$6.91^{+0.51}_{-0.80}$
5	044533.97−591441.9	10.43/10.00/36.23	<0.27	$1.29^{+0.05}_{-0.05}$	120.27/119	$22.40^{+0.82}_{-0.93}$	$7.12^{+0.26}_{-0.30}$	19.10	<0.45	$1.12^{+0.11}_{-0.11}$	38.45/30	$24.60^{+1.60}_{-3.35}$	$7.82^{+0.51}_{-1.07}$
6	044534.32−591255.7	5.03/5.10/...	<0.82	$1.87^{+0.22}_{-0.18}$	13.88/19	$8.80^{+0.58}_{-0.95}$	$2.80^{+0.18}_{-0.30}$	1.51	...	...	...	$1.36^{+0.32}_{-0.37}$	$0.43^{+0.10}_{-0.12}$
7	044535.08−591412.5	2.53/2.97/6.10	<1.32	$1.81^{+0.18}_{-0.27}$	21.18/19	$4.88^{+0.40}_{-0.53}$	$1.55^{+0.13}_{-0.17}$	3.13	<5.24	$1.33^{+0.87}_{-0.38}$	0.91/2	$3.96^{+0.65}_{-0.84}$	$1.26^{+0.21}_{-0.27}$
8	044536.73−591428.0 (B)	1.32/1.20/0.77	...	...	...	$2.48^{+0.30}_{-0.34}$	$0.79^{+0.09}_{-0.11}$	0.80	...	...	...	$0.69^{+0.21}_{-0.24}$	$0.22^{+0.07}_{-0.08}$
9	044537.00−591654.6	0.42/0.44/1.06	...	...	...	$0.34^{+0.08}_{-0.14}$	$0.11^{+0.02}_{-0.04}$	0.36	...	...	...	$0.35^{+0.21}_{-0.22}$	$0.11^{+0.07}_{-0.07}$
10	044540.38−591437.5	...	...	...	...	...	...	0.53	...	...	...	$0.42^{+0.18}_{-0.19}$	$0.13^{+0.06}_{-0.06}$
11	044540.95−591746.3	1.87/1.24/...	...	...	...	$2.52^{+0.28}_{-0.32}$	$0.80^{+0.09}_{-0.10}$	1.07	...	...	...	$1.59^{+0.52}_{-0.35}$	$0.51^{+0.17}_{-0.11}$
12	044541.76−591455.0 (C)	...	...	...	...	...	...	1.39	...	...	...	$1.18^{+0.32}_{-0.34}$	$0.38^{+0.10}_{-0.11}$
13	044542.15−591452.4 (C)	...	...	...	...	...	...	3.83	~ 0.22[d]	~ 3.36[d]	8.94/3	$3.20^{+0.66}_{-0.64}$	$1.02^{+0.21}_{-0.20}$
14	044542.41−591444.6 (C)	...	...	...	...	...	...	0.83	...	...	...	$0.73^{+0.20}_{-0.29}$	$0.23^{+0.06}_{-0.09}$
15	044542.50−591450.1 (N)	...	...	...	...	...	...	0.84	...	...	...	$1.37^{+0.51}_{-0.64}$	$0.44^{+0.16}_{-0.20}$
16	044542.61−591447.1 (C)	...	...	...	...	...	...	1.89	...	...	...	$1.59^{+0.39}_{-0.32}$	$0.50^{+0.12}_{-0.10}$
17	044542.63−591509.7	...	...	...	...	...	...	0.88	...	...	...	$0.78^{+0.19}_{-0.25}$	$0.25^{+0.06}_{-0.08}$
18	044542.71−591455.1 (C)	...	...	...	...	...	...	2.09	...	...	...	$1.73^{+0.32}_{-0.48}$	$0.55^{+0.10}_{-0.15}$
19	044544.53−591535.1	0.83/0.99/2.71	~ 0.32[d]	~ 1.84[d]	12.36/5	$1.19^{+0.12}_{-0.25}$	$0.38^{+0.04}_{-0.08}$	0.96	...	...	...	$0.82^{+0.22}_{-0.32}$	$0.26^{+0.07}_{-0.10}$
20	044546.16−591224.1	0.60/0.34/1.74	...	...	...	$0.90^{+0.15}_{-0.17}$	$0.28^{+0.05}_{-0.05}$	0.78	...	...	...	$0.61^{+0.26}_{-0.23}$	$0.19^{+0.08}_{-0.07}$
21	044546.79−591418.7	0.64/0.60/1.94	...	...	...	$1.06^{+0.11}_{-0.16}$	$0.34^{+0.03}_{-0.05}$	0.31	...	...	...	$0.23^{+0.12}_{-0.18}$	$0.07^{+0.04}_{-0.06}$
22	044549.06−591448.2	0.93/1.24/4.02	$1.46^{+1.35}_{-0.57}$	$2.87^{+0.43}_{-0.36}$	11.21/8	$1.12^{+0.14}_{-0.23}$	$0.36^{+0.05}_{-0.07}$	0.76	...	...	...	$0.64^{+0.23}_{-0.22}$	$0.20^{+0.07}_{-0.07}$
23	044549.56−591248.8	0.69/0.68/...	...	...	...	$1.44^{+0.29}_{-0.27}$	$0.46^{+0.09}_{-0.08}$	1.21	...	...	...	$1.02^{+0.27}_{-0.24}$	$0.33^{+0.09}_{-0.08}$
24	044551.00−591422.8	...	...	...	...	...	...	5.25	<1.25	$1.80^{+0.46}_{-0.25}$	4.03/6	$4.50^{+0.34}_{-1.77}$	$1.43^{+0.11}_{-0.56}$
25	044552.83−591456.1	7.77/7.15/26.82	$1.12^{+0.30}_{-0.30}$	$1.91^{+0.10}_{-0.10}$	86.23/89	$10.47^{+0.37}_{-0.46}$	$3.33^{+0.12}_{-0.15}$	31.90	$2.52^{+0.56}_{-0.49}$	$1.65^{+0.14}_{-0.13}$	42.89/51	$28.21^{+1.19}_{-6.54}$	$8.97^{+0.38}_{-2.08}$
26	044553.32−591527.9 (B)	1.05/0.77/2.83	<3.00	$1.57^{+0.41}_{-0.38}$	4.46/5	$1.78^{+0.19}_{-0.43}$	$0.57^{+0.06}_{-0.14}$	1.69	...	...	...	$1.45^{+0.25}_{-0.44}$	$0.46^{+0.08}_{-0.14}$
27	044553.78−591428.5	0.58/0.77/2.55	<1.63	$2.10^{+0.43}_{-0.40}$	1.90/3	$1.18^{+0.19}_{-0.38}$	$0.38^{+0.06}_{-0.12}$	...	...	...	...	...	...
28	044554.30−591410.5	1.34/1.60/5.47	$1.14^{+0.80}_{-0.55}$	$1.25^{+0.21}_{-0.25}$	16.04/13	$3.79^{+0.30}_{-0.72}$	$1.21^{+0.09}_{-0.23}$	3.38	<44.45	$2.51^{+2.17}_{-0.99}$	0.42/2	$4.65^{+0.77}_{-0.98}$	$1.48^{+0.24}_{-0.31}$

Notes. Sources are listed in order of increasing R.A., where N = nucleus, B = identified background galaxies, and C = sources detected in circumnuclear ring area with *Chandra* (see Table 6 for spectral fits of the integrated emission from the ring/nucleus region). Fluxes and luminosities are quoted where the source was detected in that observation (*XMM-Newton* and/or *Chandra*). For sources with >100 net counts, spectral fitting was performed with a simple power-law+absorption model and source parameters are listed. All other fluxes were measured by fitting unbinned spectra with a power law frozen to $\Gamma = 1.7$ and absorption to the Galactic value (0.223×10^{21} cm^{-2}), except the nuclear source (15), where we use $\Gamma = 1.5$.

[a] Hydrogen absorption column in units of 10^{21} cm^{-2}, including the Galactic component.

[b] Observed source flux in the 0.3–10 keV band, in units of 10^{-14} erg s^{-1} cm^{-2}.

[c] Observed source luminosity in the 0.3–10 keV band, in units of 10^{39} erg s^{-1} (assuming a distance of 16.3 Mpc).

[d] Parameter unconstrained due to high χ^2_ν.

source catalog. Three counterparts were found in the field; the offsets between the X-ray and 2MASS positions were small (0.14, 0.16, and 0.″6), and in non-uniform directions, with the greatest offset for a source 4′ off-axis at the edge of the field. Given this accuracy, no astrometric correction was made to the *Chandra* positions.

3.2. XMM-Newton Observations

NGC 1672 was observed with *XMM-Newton* for 50 ks on 2004 November 27 (ObsID 0203880101). The EPIC MOS-1, MOS-2, and PN cameras were operated with medium filters in Prime Full Window mode. Full-field light curves were accumulated for the three exposures in the 10–15 keV band to check for high-background intervals. The data were found to be clean for the duration of the observation, and the full time intervals were used in subsequent analysis: 47.9 ks (PN), 49.4 ks (MOS1), and 49.5 ks (MOS2). All data (images and spectra) were created using standard patterns corresponding to single and double pixel events for the PN (0–4), and patterns 0–12 (single to quadruple events) for the MOS cameras. For spectral extraction, the quality flag was set to zero to reject events from bad pixels and events too close to the CCD chip edges.

3.2.1. Imaging and Source Detection

Multiband source detection was performed on the PN and MOS data, using the methods detailed in Jenkins et al. (2005). In brief, images were created in the following energy bands: soft (0.3–1 keV), medium (1–2 keV), and hard (2–10 keV). Exposure maps were created for each instrument/energy band using the SAS task `EEXPMAP`, and detector masks were created for each camera with `EMASK`. Two methods of initial source recognition were used: `EBOXDETECT`, a sliding-box algorithm that simultaneously searches the three energy-band images, and `EWAVELET`, a Mexican hat wavelet detection routine that works on individual images. Both used background maps created with `ASMOOTH`. The source lists from both methods were then parameterized using `EMLDETECT`, which performs maximum likelihood PSF fits to each source. These were then compared, and any additional sources detected with `EWAVELET` were added to the `EBOXDETECT` source list, and the parameterization repeated. All sources significant at $>4\sigma$ in at least one energy band, and within the D_{25} ellipse of NGC 1672, were retained and visually inspected. Spectra, ARFs, and RMFs were extracted from the data for each source using the SAS task `especget`.

The final *XMM-Newton* catalog contains 19 extra-nuclear sources, and their properties are listed in Table 1 along with the corresponding *Chandra* properties. The source fluxes were again determined using spectral fitting (see Section 3.3). Note that six sources (including the nucleus) within the central $\sim 20''$ radius are not spatially resolved with *XMM-Newton*; these are marked with N (nucleus) and C (central region source). Apart from sources 10, 17, and 24, all other sources detected in the *Chandra* observation are detected in the *XMM-Newton* observation.

3.3. X-ray Source Spectral Fits

To estimate source fluxes reliably, we have performed spectral fitting on each source using `XSPEC` v12. Detailed spectral fitting was performed on *Chandra* sources with >100 net counts, and on *XMM-Newton* sources with >100 net counts in either the PN or MOS data. These spectra were binned (grouped to a minimum of 20 counts per bin) and fitted, using χ^2 statistics, with both power-law+absorption (PO*WABS) and disk blackbody+absorption (DISKBB*WABS) models. In all cases, the power-law model provided the best fit. Spectral parameters and corresponding 0.3–10 keV fluxes and luminosities are shown in Table 1. For the *XMM-Newton* data, the PN, MOS1, and MOS2 spectra were fitted simultaneously. The fluxes and errors from the three instruments were combined to provide a weighted mean flux for each source using the method of Barlow (2004).[14]

For sources with <100 net counts, a simple power-law+Galactic absorption model was fitted to unbinned spectra using the C-statistic (Cash 1979). Since at such low-count rates source parameters are difficult to constrain, the power-law and absorption parameters were frozen ($\Gamma = 1.7$, $N_{\rm H_{Gal}} = 0.223 \times 10^{21}$ cm^{-2}), with the normalization as the only free parameter. The resulting fluxes and luminosities are also shown in Table 1. The source properties are described in Section 4.1.

3.4. Multiwavelength Data

3.4.1. HST-ACS Observations

NGC 1672 was observed by *HST* on 2005 August 1 using the ACS Wide Field Channel (WFC) in the broadband $F435W$, $F550M$, and $F814W$ filters, plus the narrowband $F658N$ (Hα) filter. A large dither was implemented, covering the dimensions of one of the WFC chips in order to fit the visible disk of the galaxy into each observation (see Figure 1). Exposure times were 2444 s in each observation, split into four separate observations corresponding to the visibility of NGC 1672 in each single orbit. We also include in our analysis an archival ACS High Resolution Channel (HRC) $F330W$ UV observation of the nucleus of NGC 1672, taken 2002 July 19, with an exposure time of 1140 s. All of the ACS observations were processed through the standard *multidrizzle* pipeline (Koekemoer et al. 2002). As subpixel dithers were not used in the observations, the drizzle parameters pixfrac and scale were set to unity, preserving the native pixel scale of both the HRC and WFC. Each of the ACS WFC images were astrometrically registered with 2MASS stellar objects falling within the FOV, yielding an astrometric fit with an rms of $\sim 0.''15$. The $F658N$ image is significantly contaminated by continuum emission within the Hα passband; we therefore created a continuum-subtracted image (denoted as $F658CS$) using a continuum image estimated from a linear combination of the $F550M$ and $F814W$ images (weighted by their separation from the Hα line, and multiplied by the relative sensitivity of each filter to obtain the same physical units in each image).

The ACS images have a very high spatial resolution of $\sim 0.''1$. They show that, while the optical emission peaks in the central $2''$ nuclear region, it is clearly non-point like with a FWHM of $\sim$30 pixels ($1.''5$). Indeed it displays a complex/irregular morphology, and in a visual inspection we found no obvious point sources that could correspond to, for example, a nuclear star cluster (which are generally only "marginally resolved" in *HST* images of nearby galaxies; Böker et al. 2004). The complexity and extended nature of the region suggests that the use of any moderate sized photometric aperture will result in a significant overestimate of the true flux from the nucleus. We investigated this in three ways: via (1) PSF subtraction, (2) narrow aperture photometry, and (3) photometry using the *Chandra* aperture.

[14] http://www.slac.stanford.edu/~barlow/statistics.html

Table 2
Comparison of *HST*/ACS Photometry Methods for the Nucleus of NGC 1672

Filter	AB mag		
	PSF Subtraction	Narrow Aperture (0.″1 radius)	*Chandra* Aperture (1.″2 radius)
F330W	>23.5	21.54 ± 0.30	17.82 ± 0.08
F435W	>19.6	19.47 ± 0.09	16.13 ± 0.03
F550M	>19.1	18.56 ± 0.08	15.39 ± 0.03
F658N	> 18.9	17.82 ± 0.09	14.92 ± 0.04
F658CS[a]	> 19.3	18.83 ± 0.14	16.87 ± 0.04
F814W	> 17.7	17.94 ± 0.05	14.57 ± 0.03

Note. [a] Continuum-subtracted *F658N* image.

To estimate the maximum magnitude of any point source at the center of the galaxy, PSFs were constructed from isolated point sources in each image and subtracted from the centroid of the galaxy light in each band, scaled such that their cores resulted in a roughly zero flux value for the brightest pixel in the galaxy core. For two filters, it was not possible to obtain actual PSFs from the images. In the case of *F330W*, the HRC FOV is too small for any bright, isolated sources to be present, while in our *F658N* continuum-subtracted image the stars were largely subtracted. To overcome this, we used TinyTim[15] to create artificial PSFs for these filters, which were then subtracted from the data. The resulting upper limits are shown in Table 2.

An alternative to direct PSF subtraction is to measure the nuclear emission within a narrow aperture, and then apply the aperture corrections tabulated by Sirianni et al. (2005). We used a 0.″1 (2 pixel) radius aperture and subtracted the background using a 1.″2–2″ annulus centered on the nucleus. To compare directly with the *Chandra* observations, we have also performed photometry using the same physical aperture (1.″2 radius) and background annulus (again 1.″2–2″). The resulting magnitudes from these methods are also shown in Table 2.

The upper limits measured using the PSF subtraction method are similar to the measurements obtained from the narrow aperture, though there is a good deal of scatter between these and the larger *Chandra* aperture measurements. Given that PSF subtraction gives the most stringent constraints on the magnitude of a nuclear point source, we adopt these limits for the multiwavelength comparison (see Table 3), and the construction of the nuclear spectral energy distribution (SED, see Section 5.2). The AB magnitudes were converted to flux density using ABmag $= -2.5 \log F_\nu - 48.6$,[16] and then into luminosity using $\nu L_\nu = 4\pi d^2 F_\nu \times$Central filter frequency.[17] We note that the centroid of the emission in the *F330W* images does not correspond with that seen in data taken at longer wavelengths, which suggests that there is some extinction along the line of sight.

3.4.2. Spitzer IR Observations

NGC 1672 was observed with the *Spitzer* Infrared Array Camera (IRAC; Fazio et al. 2004) on 2006 November 29 (Program ID 30496; PI: Fisher). Basic calibrated data (BCD) were retrieved from the archive at 3.6, 4.5, 5.8, and 8.0 μm. We performed post-BCD processing (mosaicking, with a plate scale of 0.86 arcsec pixel^{-1}) using the *Spitzer* data-processing package MOPEX (Makovoz et al. 2006). The images are flux calibrated in the pipeline in units of surface brightness (MJy sr^{-1}), and we converted them to flux density units by multiplying by a conversion factor of 1 MJy sr^{-1} = 17.38 μJy per pixel. This is a combination of the conversion given in the *Spitzer* Observers Manual (1 MJy sr^{-1} = 23.50443 μJy arcsec^{-2}) and the pixel solid angle (0.74 arcsec^2). A multiband imaging photometer (MIPS) 24 μm calibrated image was also retrieved from the archive (from the same *Spitzer* program), which was reduced using standard pipeline processing. A stellar-continuum-subtracted 8.0 μm polycyclic aromatic hydrocarbon (PAH) image was created to highlight the star-forming regions, using a conversion based on a standard model of the starlight near-IR SED; this is 8.0 μm − 0.232 × 3.6 μm (Helou et al. 2004).

Photometry was performed on the nuclear source in the four IRAC bands using a 1.″5 radius aperture centered on the *Chandra* position of the nucleus, using a local annular background between 2.″5 and 3.″0. This aperture was chosen because of the larger PSF of IRAC (1.″4–1.″7 FWHM; Fazio et al. 2004), and aperture corrections were applied as detailed in the IRAC Data Handbook v3.0, Section 5.5.1. The resulting flux densities (and AB magnitudes) are shown in Table 3. Note that photometry is not performed on the MIPS data, as the spatial resolution (∼6″) is insufficient to separate the nuclear source from the circumnuclear ring emission.

3.4.3. Radio Observations

Radio continuum observations of NGC 1672 were obtained at 3 cm and 6 cm with the ATCA. Data reduction was carried out with the MIRIAD[18] software package, using standard procedures.

The 3 cm image was created using archival data from a 1.5C configuration obtained in 2003 May and a 6D configuration obtained in 2003 July, with on-source integration times of 9 hr and 10 hr, respectively. Both observations consist of two frequency bands centered at 8640 MHz and 8768 MHz, with bandwidths of 128 MHz divided into 32 channels. At 8700 MHz, the ATCA primary beam is 5.′5. The data for both observations/frequency bands were combined using "robust" weighting ($r = 0$), resulting in an angular resolution of 1.″3 × 1.″0 and an rms of 0.03 mJy beam^{-1}. The 6 cm image was created using archival data in the 6A configuration obtained in 2002 May, with an on-source integration time of 11 hr. The observation consists of two frequency bands centered at 4800 MHz and 4928 MHz, with bandwidths of 128 MHz divided into 32 channels. At 4864 MHz the ATCA primary beam is 9.′8. The data from both frequency bands were combined, resulting in an angular resolution of 1.″9 × 1.″7 and an rms of 0.04 mJy beam^{-1}. The source PKS B1934–638 was used as the primary (amplitude and bandpass) calibrator, and PKS B0522–611 and PKS B0420–625 were used as the secondary (phase) calibrators at 3 and 6 cm, respectively.

A point source fit to the nuclear source gives a position of α, δ(J2000) = $04^h45^m42^s.50$, $-59°14'49''.85$ (±0.″12). We measure peak fluxes of 0.95 ± 0.15 mJy at 3 cm and 1.62 ± 0.15 mJy at 6 cm. We measure integrated flux densities of 34 mJy (3 cm) and 35 mJy (6 cm) for the radio continuum emission from both the nuclear source and surrounding star-forming ring. It is likely that some extended flux has been resolved out by the interferometer. Single-dish radio continuum flux estimates of NGC 1672 (PMN J0445–5914, PKS J0445–5915) at ∼5 GHz

[15] http://www.stecf.org/instruments/TinyTim/
[16] http://www.stsci.edu/hst/acs/analysis/zeropoints
[17] http://acs.pha.jhu.edu/instrument/filters/general/Master_Table.html
[18] http://www.atnf.csiro.au/computing/software/miriad/

Table 3
Multiwavelength Photometry of the Nuclear Source in NGC 1672

Filter	AB mag	Flux Density (mJy)	ν (Hz)	νL_ν (erg s^{-1})
		HST/ACS Optical/UV		
F330W	>23.5	<0.001	8.94×10^{14}	$<4.1 \times 10^{38}$
F435W	>19.6	<0.053	6.98×10^{14}	$<1.2 \times 10^{40}$
F550M	>19.1	<0.082	5.38×10^{14}	$<1.4 \times 10^{40}$
F658N	>18.9	<0.105	4.56×10^{14}	$<1.5 \times 10^{40}$
F658CS[a]	>19.3	<0.069	4.56×10^{14}	$<1.0 \times 10^{40}$
F814W	>17.7	<0.302	3.60×10^{14}	$<3.5 \times 10^{40}$
		Spitzer/IRAC Near-IR		
3.6 μm	13.95 ± 0.02	9.52 ± 0.16	8.45×10^{13}	$2.56 \pm 0.04 \times 10^{41}$
4.5 μm	14.40 ± 0.03	6.31 ± 0.13	6.68×10^{13}	$1.34 \pm 0.03 \times 10^{41}$
5.8 μm	14.62 ± 0.11	5.13 ± 0.38	5.23×10^{13}	$8.54 \pm 0.63 \times 10^{40}$
8.0 μm	14.16 ± 0.08	7.87 ± 0.35	3.81×10^{13}	$9.53 \pm 0.43 \times 10^{40}$
		ATCA Radio		
5 GHz (6 cm)	...	1.62 ± 0.15	4.80×10^{9}	$2.47 \pm 0.23 \times 10^{36}$
10 GHz (3 cm)	...	0.95 ± 0.15	8.64×10^{9}	$2.61 \pm 0.41 \times 10^{36}$

Note. [a] Continuum-subtracted *F658N* image.

(6 cm) are typically around 100 mJy (see Wright et al. 1994; Harnett 1987).

There is one other radio source in the FOV at α, δ(J2000) = $04^h45^m36^s.70$, $-59°14'28''.00$ ($\pm 0''.03$), with flux densities of 1.5 ± 0.1 mJy (3 cm) and 1.4 ± 0.1 mJy (6 cm). This is positionally coincident with X-ray source 8 (044536.73–591428.0).

4. RESULTS

Figures 2(a)–(c) show three-color *Chandra*, *XMM-Newton,* and *Spitzer*/IRAC images of the entire D_{25} area of NGC 1672. The X-ray sources outside the nuclear region are well resolved in both the *Chandra* and *XMM-Newton* data, and are discussed in Section 4.1. There is also a diffuse hot X-ray gas component, which is shown in Figure 2(d) as extended red/green X-ray emission (see Section 4.2). The nuclear region is very bright at all wavelengths and will be discussed in detail in Section 4.3. The *Spitzer* IR data show that the majority of the non-nuclear star formation activity is confined to the bar and inner spiral arms (illustrated in red and green), whereas older stellar populations are spread throughout the disk (illustrated in blue). Figure 3 shows the high-resolution three-color *HST*/ACS image, where the bar structure, numerous H II regions, and dust lanes are visible.

4.1. X-ray Point Source Population

Figure 4 (top left) shows the DSS optical image of NGC 1672, overlaid with the positions of the 28 X-ray sources detected within the D_{25} area of the galaxy (blue crosses). Note that we do not plot the source positions on the *HST* image here since it does not cover the entire D_{25} area. The positions correlate well with the optical structure of the galaxy, with sources concentrated in the nuclear region (see Section 4.3) and spread throughout the disk and spiral arms. The extranuclear source fluxes range between $F_X = 2.3 \times 10^{-15}$and 2.8×10^{-13} erg s^{-1} cm^{-2} over both *XMM-Newton* and *Chandra* observations, corresponding to $L_X = 7.4 \times 10^{37}$–9.0×10^{39} erg s^{-1} at the distance of NGC 1672.

Nine sources, almost a third of the population, reach ultraluminous X-ray source (ULX) luminosities ($L_X > 10^{39}$ erg s^{-1}, 0.3–10 keV) in either one or both X-ray observations; these are marked with red circles (sources 1, 4, 5, 6, 7, 13, 24, 25, and 28). Three of the ULXs are very bright (sources 4, 5, and 25 with $L_X > 5 \times 10^{39}$ erg s^{-1}, marked with larger circles), and are co-spatial with the ends of the bar (as previously noted by Brandt et al. 1996). This is consistent with models that show that gas can accumulate at the tips of bars due to the co-rotation of the bar structure with the disk (Englmaier & Gerhard 1997), thereby creating star-forming regions where XRBs can form. Other examples of this phenomenon have been observed in the barred galaxies NGC 7771 (Jenkins et al. 2005) and NGC 4303 (Jiménez-Bailón et al. 2003).

Figure 4 (top right) shows the source positions overlaid on the *Spitzer* 8 μm image, illustrating the coincidence of many X-ray sources with regions of star formation in the bar and inner spiral arm regions. We have correlated the X-ray source positions with the H II region catalog of Evans et al. (1996). Taking into account both the absolute astrometric accuracy of the X-ray and H II region positions ($\sim 1''$ combined) as well as the measured areas of the H II regions, we associate 11 X-ray sources with H II regions (sources 2, 4, 5, 7, 13, 14, 18, 21, 25, 27, and 28). These include the three brightest ULXs and three sources in the circumnuclear ring.

We have not performed any complex spectral fitting on the X-ray sources, as even the brightest are well fit with simple absorption+power-law models, with χ^2_ν close to one (see Table 1). The spectra and model fits are shown in Figures 5 and 6. However, we note that even though this simple model provides acceptable empirical fits to these data, this is likely due to the relatively low photon counts ($\lesssim$2000 counts, total PN+MOS or ACIS-S), and the true underlying spectral shapes are likely to be more complex (see Stobbart et al. 2006 for a discussion).

Figure 4 (top left) also denotes variable sources (marked with white squares). Six sources show significant long-term flux variability between the *XMM-Newton* and *Chandra* observations at levels of $>2.5\sigma$; these are sources 1, 4, 6, 8, 21, and 25. Most notable are the increases in flux in two of the brightest ULXs in the *Chandra* observations; source 4 increases by a factor of $\sim$5 (up to 6.9×10^{39} erg s^{-1}) and source 25 increases by a factor of $\sim$3 (up to 9.0×10^{39} erg s^{-1}), indicating that the high luminosity of

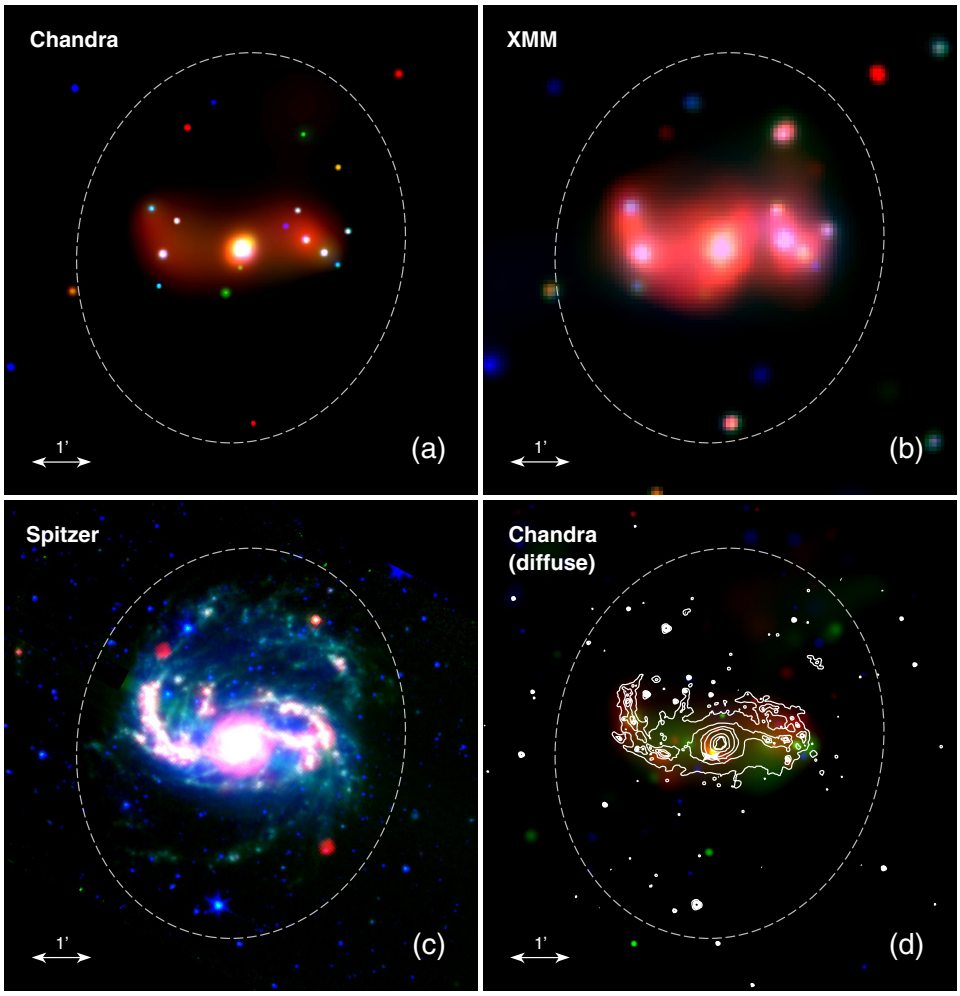

Figure 2. (a) *Chandra* three-color ACIS-S image of NGC 1672: red = 0.3–1 keV, green = 1–2 keV, and blue = 2–10 keV. (b) *XMM-Newton* EPIC (MOS1+MOS2+PN) three-color image (in the same energy bands). (c) *Spitzer* three-color image: red = 24 μm (MIPS), green = 8 μm (IRAC), and blue = 3.6 μm (IRAC). (d) *Chandra* three-color image of the diffuse X-ray emission. Contours from the *Spitzer*/IRAC stellar-continuum-subtracted 8 μm data are overlaid, which are spatially correlated with the X-ray emission. The D_{25} ellipse of the galaxy is shown with a dashed white line. All images are on the same scale and co-aligned. North is up and east is to the left.

(A color version of this figure is available in the online journal.)

these sources is not due to confusion of several fainter sources. These flux increases are accompanied by a spectral hardening of source 4, but no significant spectral change in source 25. The other four sources with spectral fits in both observations show no significant spectral change between observations. Another four sources (10, 17, 24, and 27) are detected in only one observation.

To investigate longer-term behavior, in Table 4 we show a comparison between *XMM-Newton*, *Chandra,* and *ROSAT*/HRI soft X-ray luminosities for five sources detected in all three observations. We quote the 0.2–2 keV HRI luminosities from de Naray et al. (2000) for the combined 1992/1997 data set (which gives better photon statistics), together with 0.2–2 keV luminosities derived from the best-fit *XMM-Newton* and *Chandra* spectral models corrected for Galactic absorption. Note that we also include source 23 (*ROSAT* source X-5), which was originally believed to be coincident with a foreground star given the *ROSAT* positional errors ($\sim$5″). However, with the *Chandra* positional accuracy of $\sim$0.″5, we show that this source is not consistent with the 2MASS position of the star ($04^{h}45^{m}49\overset{s}{.}54$, $-59^{\circ}12'54\overset{''}{.}1$) with an offset of $\sim$5″. In fact, this is the source that shows the largest long-term variability with $L_{\rm high}/L_{\rm low} = 3.6$ over this $\sim$10 year period. The remaining sources vary in luminosity by factors of 1–3.

Table 4
Comparison with *ROSAT*/HRI X-ray Source Luminosities

Source	*XMM-Newton* L_X (0.2–2 keV) (erg s^{-1})	*Chandra* L_X (0.2–2 keV) (erg s^{-1})	*ROSAT*	*ROSAT*/HRI L_X (0.2–2 keV) (erg s^{-1})
2	$1.16^{+0.28}_{-0.32} \times 10^{38}$	$1.49^{+0.31}_{-0.29} \times 10^{38}$	X-9	$2.90 \pm 1.54 \times 10^{38}$
4	$7.92^{+0.51}_{-0.81} \times 10^{38}$	$2.48^{+0.02}_{-0.03} \times 10^{39}$	X-7	$8.20 \pm 1.97 \times 10^{38}$
5	$2.03^{+0.05}_{-0.10} \times 10^{39}$	$1.91^{+0.01}_{-0.03} \times 10^{39}$	X-3	$2.10 \pm 0.28 \times 10^{39}$
23	$3.27^{+0.71}_{-1.19} \times 10^{38}$	$1.60^{+0.39}_{-0.35} \times 10^{38}$	X-5	$5.72 \pm 1.80 \times 10^{38}$
25	$1.37^{+0.06}_{-0.07} \times 10^{39}$	$2.99^{+0.02}_{-0.03} \times 10^{39}$	X-2	$2.20 \pm 0.28 \times 10^{39}$

Notes. *ROSAT* source luminosities are taken from de Naray et al. (2000) and are corrected for Galactic absorption. *XMM-Newton* and *Chandra* luminosities are calculated in the *ROSAT* 0.2–2 keV band from their best-fit spectral models and are also corrected for Galactic absorption for direct comparison with the *ROSAT* results.

We estimate the number of background X-ray sources in the D_{25} area of NGC 1672 using the hard band (2–10 keV) log N–log S source distributions from *Chandra* deep field studies (we do not use the soft band log N–log S since the detection sensitivity at soft energies will be affected by absorption by neutral material

Figure 3. *HST*/ACS three-color image of NGC 1672, produced by Zolt Levay at the Space Telescope Science Institute. The colors correspond to red=combined *F658N* (Hα) + *F*814*W* (*I*), green = *F*550*M*(*V*), and blue = *F*435*W* (*B*). The image is 4.′4 × 3.′2 in size, with an orientation such that north is 34° east (left) of the *y*-axis.

(A color version of this figure is available in the online journal.)

in the galactic disk). Using a source detection threshold of 12 counts in the 0.3–10 keV band (corresponding to the faintest source detected in the *Chandra* observation), and converting this to a 2–10 keV flux for a typical AGN ($\sim 1.5 \times 10^{-15}$ erg s^{-1} cm^{-2}, using $\Gamma = 1.7$ and $N_{\rm H_{Gal}} = 0.223 \times 10^{21}$ cm^{-2}), the log N–log S relations of Giacconi et al. (2001), Campana et al. (2001), and Bauer et al. (2004) all predict between two and three background sources in the field. Note that this is in fact an upper limit, since the NGC 1672 source catalog is not corrected for incompleteness. Inspection of the *HST*/ACS images allows us to identify two X-ray sources as background galaxies immediately; these are source 26, which appears to be a face-on disk galaxy with a bright nucleus, and source 8, which looks like an edge-on galaxy with visible dust lanes seen through the disk of NGC 1672 (see Figure 4, lower panel). As noted in Section 3.4.3, source 8 is the only extranuclear X-ray source with a detected radio counterpart. At the distance of NGC 1672, the 2–10 keV X-ray luminosity (at its brightest in the *XMM-Newton* observation) would be $L_{\rm X} = 7.9 \times 10^{38}$ erg s^{-1}, and the 5 GHz radio luminosity would be $\nu L_\nu = 2.2 \times 10^{36}$ erg s^{-1}. According to the X-ray/radio fundamental plane of Merloni et al. (2003), this is inconsistent with emission from a stellar mass black hole (i.e., too radio bright), and supports the hypothesis that this source is a background AGN (see Section 5 for further discussion of this relation with regards to the nuclear source).

4.2. Diffuse X-ray Emission

We have used the *Chandra* observation to study the diffuse X-ray component of NGC 1672 due to its $\sim 1''$ spatial resolution, and hence ease of source subtraction. The morphology of the diffuse emission is illustrated in Figure 2(d), where the X-ray point sources and central ring region have been masked, and the residual emission adaptively smoothed. Overlaid are contours from the continuum-subtracted *Spitzer*/IRAC 8.0 μm image, which highlights star formation activity; the diffuse emission is spatially correlated with the IR emission, following the bar/inner spiral arm structure.

A source spectrum was extracted from an elliptical region $(a, b) = (2.'25, 1.'11)$ centered on the nucleus with a position angle of 90°. The detected point sources were excluded (using regions with twice the radius of the 90% encircled energy ellipses), as well as the innermost 20″ radius circumnuclear ring region. The background regions were chosen to be (1) the region on the ACIS-S3 chip outside the D_{25} radius and not containing point sources and (2) the region on the ACIS-S1 chip not containing bright point sources. To further constrain the soft end of the background emission, we also used the seven element *ROSAT* All Sky Survey (RASS) SED (Snowden et al. 1997) from an annulus $30' < R < 1°$ around NGC 1672, extracted using the X-ray background web tool hosted by

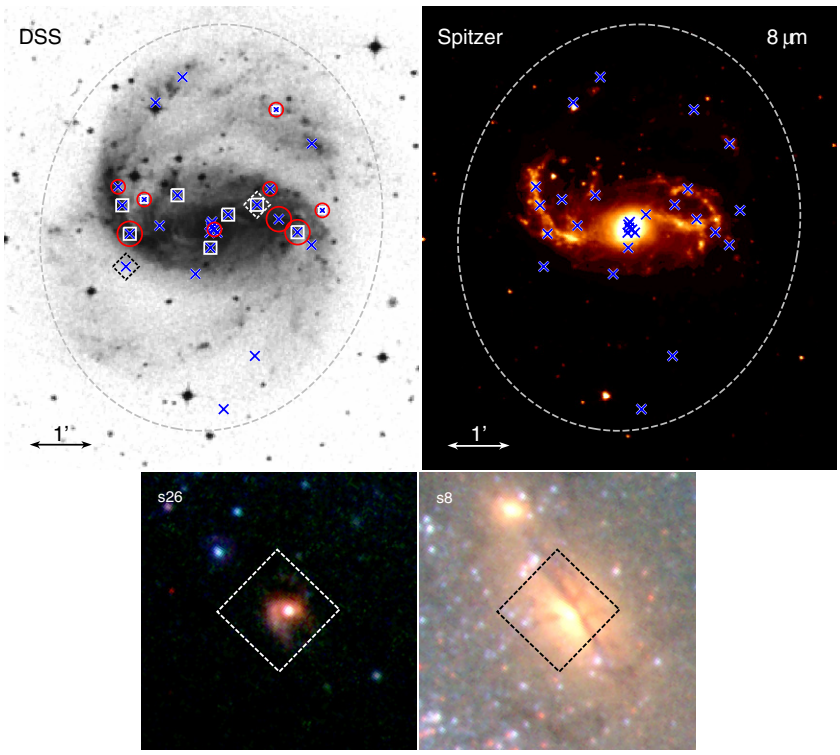

Figure 4. Top left: DSS optical image of NGC1672 with the 28 X-ray source positions marked with blue crosses. Sources with $L_X > 10^{39}$ erg s^{-1} in the 0.3–10 keV band (i.e., ULXs) in either the *XMM-Newton* or *Chandra* observation are marked with red circles, with the three brightest ($L_X > 5 \times 10^{39}$ erg s^{-1}) denoted by larger circles (sources 4, 5, and 25). Sources that show variability of $>2.5\sigma$ between the two observations are also marked with white squares (including sources detected in only one observation). The dotted diamonds denote sources 8 and 26, which are resolved as background galaxies in the optical *HST*/ACS images; these are shown in the lower panel, where the diamond boxes are $2'' \times 2''$ centered on the X-ray positions. Top right: the *Spitzer*/IRAC continuum-subtracted 8 μm image, showing the locations of the X-ray sources with respect to star-forming regions in the galaxy.

(A color version of this figure is available in the online journal.)

the HEASARC.[19] For each *Chandra* spectrum, we created a particle background spectrum using the "stowed" data from the appropriate chip and mode, scaled to produce the same 10–13 keV band count rate as observed in the ObsID 5932 data. The particle background spectra were then used as the "background" spectra within XSPEC, and the spectra of the galaxy and the remainder of the background emission were fitted simultaneously. After subtraction of the particle background, there were 1580 counts in the source spectrum and 2890 counts in the background spectra. The spectra and fits are shown in Figure 7, and the fit parameters for both background and galaxy emission are shown in Table 5.

The emission in the background regions consists of Galactic foreground emission from the Local Hot Bubble (LHB) and the Galactic halo (modeled with APEC components), the extragalactic background due to unresolved AGN (modeled with a power law), as well as contributions from soft protons. The Galactic halo and the extragalactic background are absorbed by the total neutral column along the line of sight (0.223×10^{21} cm^{-2}). The abundances were fixed to the Wilms et al. (2000) solar values. The photon index of the power law was set to 1.46 (Chen et al. 1997), while the normalization of each spectrum was initially set to the value predicted by the point source detection limit, a total background value of 11.6 photons cm^{-2} s^{-1} sr^{-1} keV^{-1} at 1 keV (De Luca & Molendi 2004), and the 0.5–2.0 keV luminosity function of Mateos et al. (2008). The normalizations of the power laws were then allowed to vary, and the fitted values were not too different from the initial values. A soft proton component was also included in the fit, which can be represented by a flat ($\Gamma = 0$) power law with an exponential cutoff at 500 keV (Kuntz & Snowden 2010).

The galaxy emission was fit with MEKAL thermal plasma models, split into components representing the unabsorbed emission coming from the front of the galactic disk, and absorbed emission coming from behind the disk, with their temperature parameters tied. Adequate fits could not be obtained from a single temperature model. We found that a two-component model provided a very good fit, but cannot rule out the existence of a distribution of temperatures or non-equilibrium plasmas (see the discussion in Kuntz & Snowden 2001). The temperatures ($kT = 0.22/0.77$ keV) are typical of those found in galactic disks, with a ratio of emission measures typical of late-type galaxies. The abundance of the galaxy was assumed to be solar (Storchi-Bergmann et al. 1996), and due to the uncertainty introduced by the intermixture of absorption and emission components, the disk absorption column density was initially set to zero and allowed to vary freely. In Table 5, we show fitted values for two different cases, the first assumes no absorbing galactic disk, and the second allows the absorbing column within the galaxy to vary. The final fitted value for the disk absorption was 5.48×10^{21} cm^{-2}, rather higher than a typical galactic disk, and which implies a near complete absorption of the flux from the far side of the disk. However, since the spectrum was extracted from the bar region, this value may not be unreasonable. The galactic absorption does not significantly change the fitted temperatures, and the normalizations vary by roughly a factor of two, as one might expect given the strong fitted absorption. The total 0.5–2 keV luminosity of the diffuse components is

[19] http://heasarc.gsfc.nasa.gov/cgi-bin/Tools/xraybg/xraybg.pl

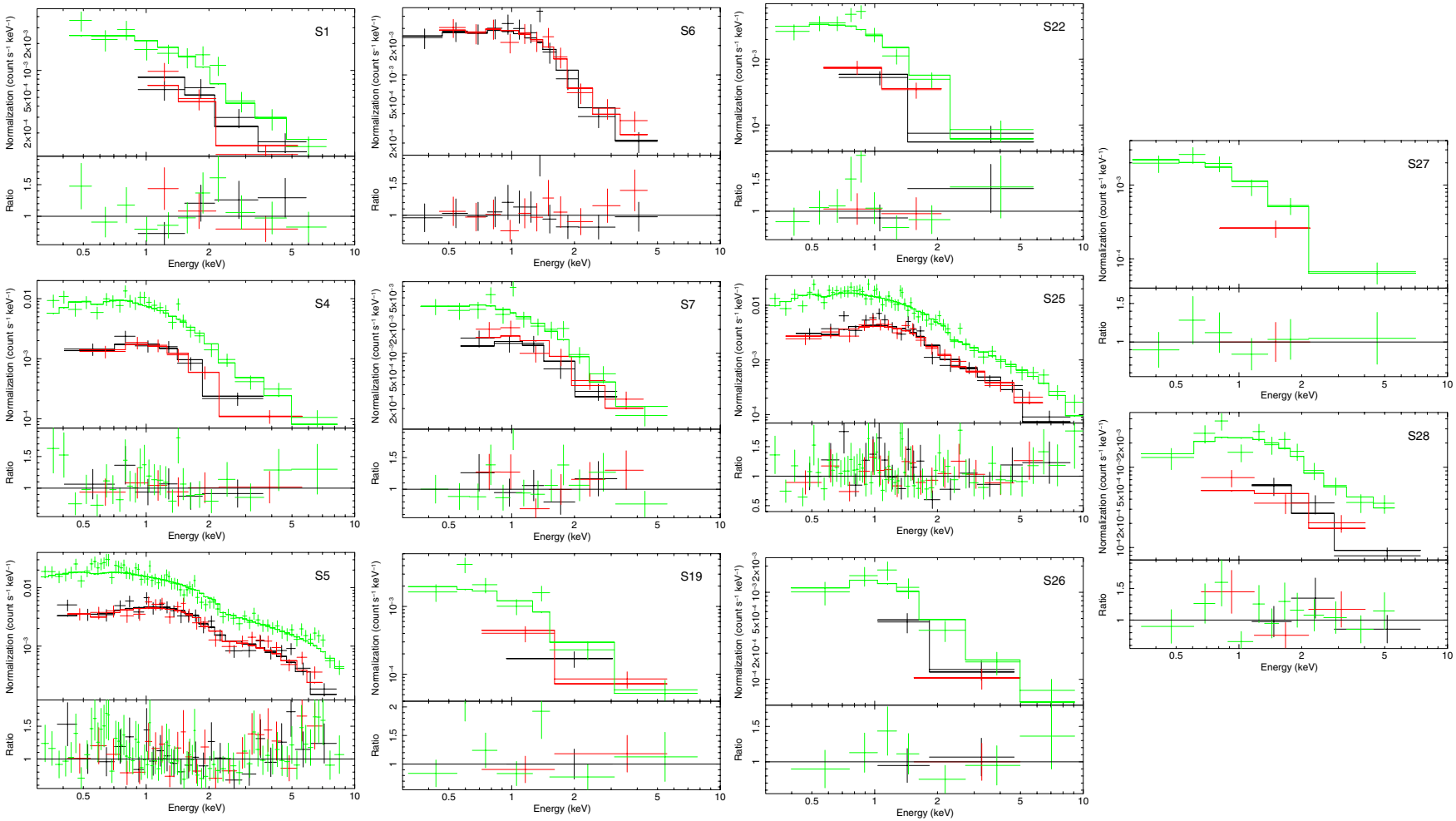

Figure 5. *XMM-Newton* EPIC spectra of the 11 sources with >100 net PN or MOS counts. PN data points and power-law+absorption models are shown in green; those of the MOS data are shown in red/black. (A color version of this figure is available in the online journal.)

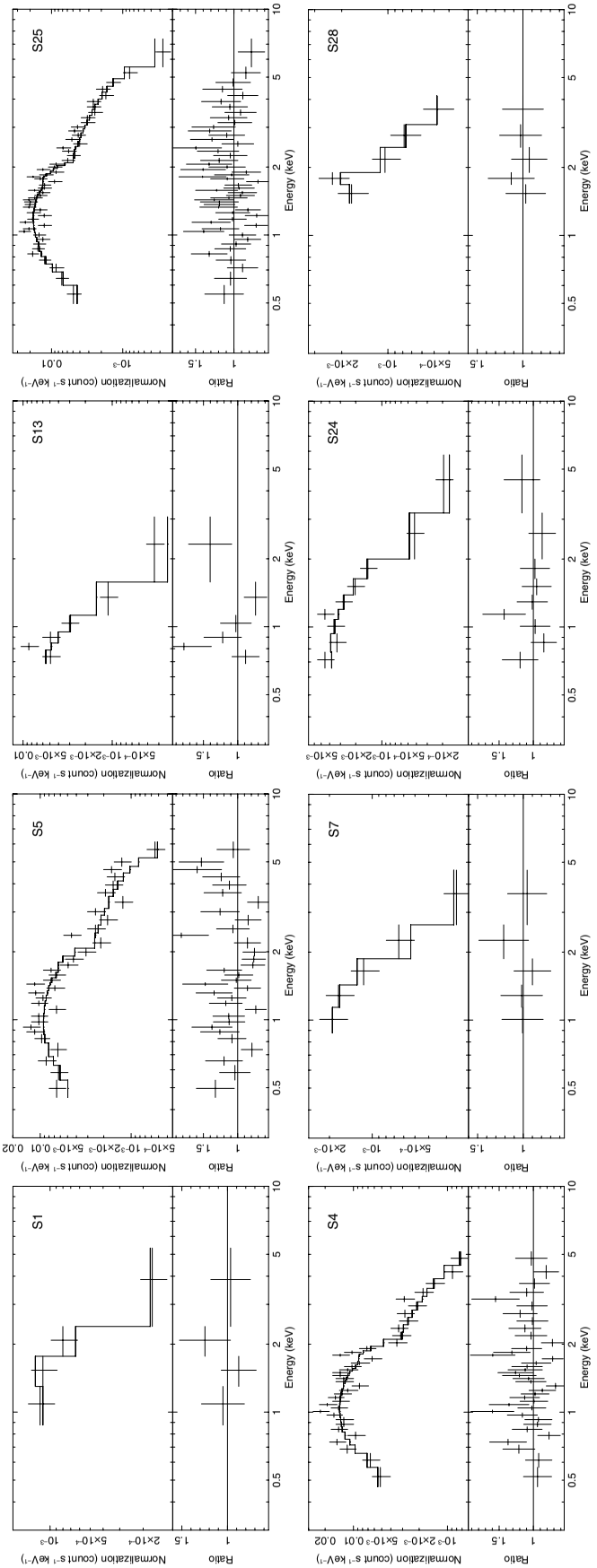

Figure 6. *Chandra* ACIS-S spectra of the eight sources with >100 net counts, together with the power-law+absorption models.

Table 5
Chandra Diffuse Emission and Galactic Foreground Spectral Fits

Parameter	$N_{\rm H} = 0.0$ cm^{-2}	$N_{\rm H} = 5.48 \times 10^{21}$ cm^{-2}	Units
Galactic Foreground: APEC$_l$+WABS*(APEC$_d$+PO)			
kT_l	$0.12^{+0.01}_{-0.01}$	$0.12^{+0.01}_{-0.01}$	keV
N_l	$1.61^{+0.07}_{-0.05}$	$1.62^{+0.07}_{-0.07}$	10^{-2} cm^{-6} pc
kT_d	$0.57^{+0.10}_{-0.10}$	$0.48^{+0.18}_{-0.15}$	keV
N_d	$0.17^{+0.04}_{-0.03}$	$0.19^{+0.04}_{-0.06}$	10^{-2} cm^{-6} pc
NGC 1672: MEKAL$_s$+MEKAL$_h$+WABS*(MEKAL$_s$+MEKAL$_h$)			
kT_s	$0.22^{+0.02}_{-0.01}$	$0.22^{+0.02}_{-0.03}$	keV
N_s	$2.17^{+0.25}_{-0.25}$	$4.39^{+0.57}_{-0.44}$	10^{-2} cm^{-6} pc
kT_h	$0.78^{+0.26}_{-0.13}$	$0.77^{+0.39}_{-0.16}$	keV
N_h	$0.72^{+0.16}_{-0.19}$	$1.12^{+0.29}_{-0.41}$	10^{-2} cm^{-6} pc
$N_{\rm H}$	0 (fixed)	$5.48^{+2.78}_{-1.67}$	10^{21} cm^{-2}
χ^2/dof	310.6/268	307.7/260	
F_{X_s}	$9.09^{+1.05}_{-1.05}$	$9.84^{+1.28}_{-0.98}$	10^{-14} erg s^{-1} cm^{-2}
F_{X_h}	$4.72^{+1.01}_{-1.23}$	$4.67^{+1.20}_{-1.70}$	
L_{X_s}	$3.28^{+0.38}_{-0.38}$	$6.56^{+0.85}_{-0.65}$	10^{39} erg s^{-1}
L_{X_h}	$1.61^{+0.34}_{-0.41}$	$2.52^{+0.65}_{-0.91}$	

Notes. For the Galactic foreground fits, l = Local Hot Bubble (LHB) component and d = Galactic Halo component. For the NGC 1672 diffuse emission fits, s = soft (lower temperature) component and h = hard (higher temperature) component. PO is the power-law continuum model, and APEC/MEKAL are thermal plasma models (solar abundances), where N is the emission measure. Model parameter errors correspond to 90% confidence limits for one parameter of interest. The soft and hard observed fluxes are quoted in the 0.5–2.0 keV band, and the unabsorbed luminosities are shown for each model (assuming a distance of 16.3 Mpc), corrected for both Galactic and intrinsic absorption.

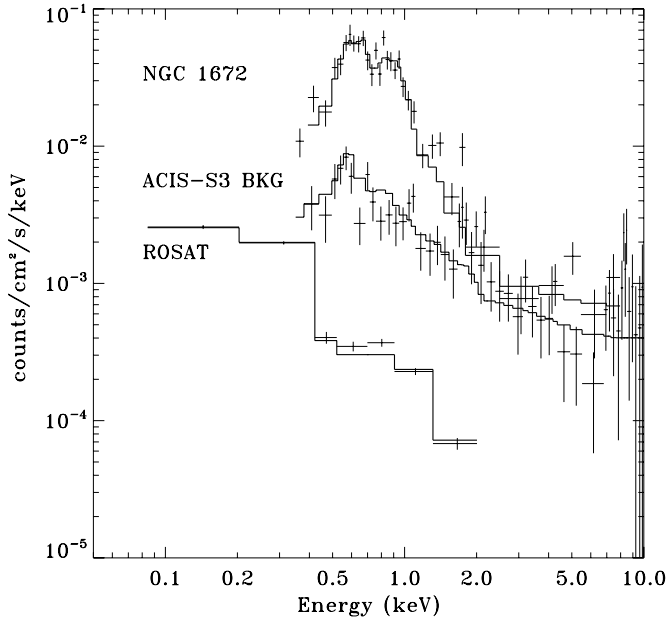

Figure 7. *Chandra* ACIS spectral data and fit for the diffuse galaxy spectrum, the Galactic foreground/extragalactic background, and RASS data. The ACIS-S1 background spectrum is not shown for clarity.

4.9×10^{39} erg s^{-1} for the model with no intrinsic absorption, and 9.0×10^{39} erg s^{-1} for the model with high disk absorption (see Table 5).

In order to place a spectroscopic limit on the contribution to this emission from unresolved point sources, we introduced an absorbed power-law component to the model with no intrinsic absorption, fixing the photon index to 1.7, but allowing the absorption and normalization to vary. The best fit allowed allowed a luminosity of 1.2×10^{39} erg s^{-1} (0.5–2 keV) to be due to unresolved sources, with a 90% upper limit of 2.4×10^{39} erg s^{-1}.

4.3. Nucleus: Images and X-ray Photometry

The new high-resolution data allow us to probe the nuclear structure of NGC 1672 on sub-kpc scales. Figure 8 shows images of the central region of the galaxy in the X-ray, optical and 3 cm radio bands. For the first time, the *Chandra* images (Figure 8(a)) spatially resolve the X-ray emission into a weak point source (source 15) surrounded by the circumnuclear ring (white polygons highlight the detected point sources in the region). The *HST*/ACS data (Figure 8(b)) also show that NGC 1672 possesses a nuclear spiral, which is one of the candidate fueling mechanisms for AGN (Martini et al. 2003). The radio data clearly show both the ring and a compact nuclear source (Figure 8(c)), and in the *Spitzer*/IRAC image (Figure 8(d)) strong star-forming activity is seen in the ring (8.0 μm, green), while the region inside the ring is dominated by older stars (3.6 μm, blue). The nucleus itself shows evidence of a combination of the two (note there is still some PAH emission in the nucleus itself).

In Figure 8(e), radio contours are overlaid on the *Chandra* image, which illustrates a strong spatial correlation between both the ring and position of the nuclear source. The X-ray position of the nucleus agrees with the radio position to within 0.″25. The *Chandra* X-ray contours are overlaid on the Hα image in Figure 8(f), and show a correlation between the location of the circumnuclear ring and the outer edge of the nuclear spiral. The central X-ray source is also spatially coincident with the peak of the Hα emission.

The nucleus is only detected in the medium band (1–2 keV, 18 net counts) and hard band (2–10 keV, 17 net counts)

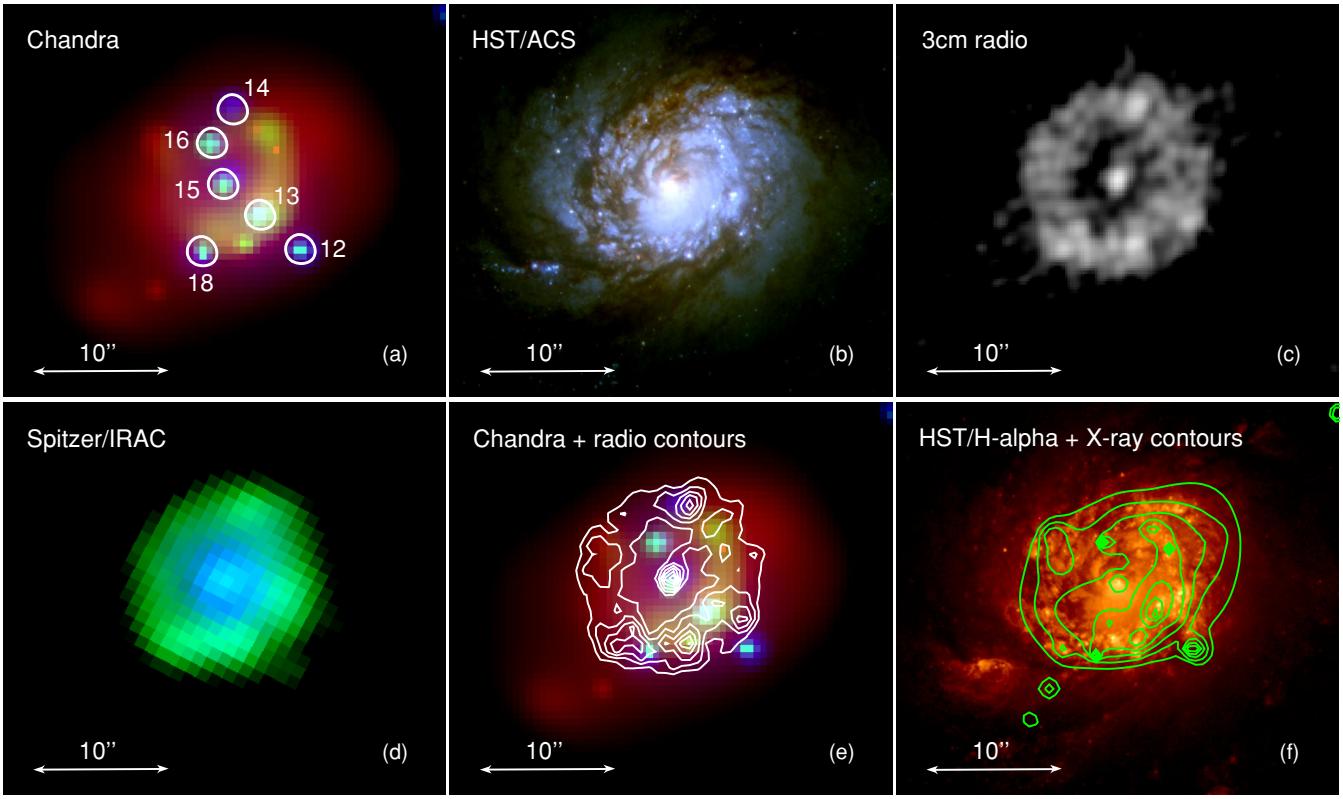

Figure 8. Circumnuclear region of NGC 1672. (a) *Chandra* three-color image: red = 0.3–1 keV, green = 1–2 keV, and blue = 2–10 keV. The circumnuclear ring is evident, surrounding a weak nuclear X-ray point source (15). The white polygons denote the 90% extraction regions of the detected point sources. (b) *HST*/ACS three-color image: red = combined *F*658*N* (Hα) + *F*814*W* (*I*), green = *F*550*M* (*V*), and blue = F435W (*B*). (c) 3 cm ATCA radio image. (d) *Spitzer*/IRAC two-color image: green = 8 μm, blue = 3.6 μm. (e) *Chandra* three-color image with ATCA 3 cm radio contours overlaid. (f) *HST* Hα image with *Chandra* broadband (0.3–10 keV) contours overlaid. All images are on the same scale and co-aligned. North is up and east is to the left.

(A color version of this figure is available in the online journal.)

in the *Chandra* observation, indicating that there is some obscuring material along the line of sight. To estimate the spectral shape (and hence source flux) of the nucleus, an X-ray hardness ratio was calculated using the BEHR algorithm (Park et al. 2006). This is a Bayesian method that takes into account the Poissonian nature of low-count data, and deals with situations where no net source counts are detected in one or more bands (as is the case here in the soft band). The hardness ratio is plotted on a model grid in Figure 9, and indicates that the source is hard ($\Gamma = 1.5^{+1.0}_{-0.8}$) with fairly low absorption ($N_{\rm H} \sim 5 \times 10^{21}$ cm^{-2}). This translates into an unabsorbed 2–10 keV luminosity of only $L_{\rm X} \sim 3.9 \times 10^{38}$ erg s^{-1}. If we use the upper limit to the absorption in the flux calculation ($N_{\rm H} \sim 1.5 \times 10^{22}$ cm^{-2}), the luminosity is only marginally increased to $L_{\rm X} \sim 4.2 \times 10^{38}$ erg s^{-1}. This is very faint for a Seyfert galaxy, but does just fall into the range found in the LLAGN survey of Ho et al. (2001) ($L_{\rm X} \sim 10^{38}$–10^{41} erg s^{-1}). However, we have adopted a very simple model here; more complex models may admit a significantly higher absorption column density (see Section 5.3 for further discussion).

4.4. Nuclear Region: X-ray Spectroscopy

Figure 10 (top and middle) shows *XMM-Newton* spectra of the central 22″ radius region of the galaxy, which includes all contributions from the nucleus and circumnuclear ring. The spectra contain ∼10,500 background-subtracted counts in total; ∼6700 counts in the PN data, ∼1800 counts in the MOS1 data, and ∼2000 counts in the MOS2 data. The data were fit simultaneously with two- and three-component spectral models, with combinations of a power law, to model the non-thermal contributions from accreting sources (XRBs/AGN), and MEKAL thermal plasma components to model the hot gas (see Table 6). The simplest model (MEKAL+PO with equal absorbing columns, model 1) yields a reasonable fit ($\chi^2_\nu \sim 1.3$), with a gas temperature of 0.60 keV and a soft power-law component ($\Gamma = 2.27$). To improve this, we fitted the data with three-component models. We tried a model where all absorption columns were tied (model 2) and one where each component had its own absorption (model 3). Of the two, model 3 provides a slightly superior fit ($\chi^2_\nu \sim 1.16$), with thermal temperatures of $kT =$ 0.24/0.60 keV) and a soft power law ($\Gamma = 2.17^{+0.09}_{-0.09}$). The thermal components in this model show increasing absorption with increasing temperature, a pattern found previously in some starburst galaxies (e.g., Lira et al. 2002; Jenkins et al. 2005). However, we have frozen the value for the power-law absorption to 0.5×10^{21} cm^{-2} (0.72×10^{21} cm^{-2} including Galactic absorption), the value we get for model 2 where there is only one absorption column for the whole model; if the absorption is left free in model 3 it tends to zero, which is not realistic if the point sources are related to the same stellar population as the thermal components. The addition of the cooler MEKAL component produces a substantial improvement to the fit, with a $\Delta\chi^2$ of 43 for three additional degrees of freedom (dof). Note that the temperatures of the thermal components are consistent with those measured in the diffuse emission analysis (Section 4.2),

Table 6
XMM-Newton Spectral Fitting Results for the Central 22″ Radius Region (Nucleus + Ring)

Power Law		MEKAL$_s$		MEKAL$_h$		χ^2/dof	F_X[b]	L_X[c]
N_H[a]	Γ	N_H[a]	kT_s (keV)	N_H[a]	kT_h (keV)			
Model 1: WABS*(PO+MEKAL$_h$)								
$0.59^{+0.13}_{-0.09}$	$2.27^{+0.11}_{-0.10}$	...	...	[d]	$0.60^{+0.01}_{-0.01}$	435.8/343	$3.07^{+0.08}_{-0.09}$	$12.29^{+0.27}_{-0.29}$
Model 2: WABS*(PO+MEKAL$_s$+MEKAL$_h$)								
$0.76^{+0.13}_{-0.10}$	$2.21^{+0.10}_{-0.09}$	[d]	$0.20^{+0.05}_{-0.02}$	[d]	$0.61^{+0.02}_{-0.02}$	401.4/341	$3.01^{+0.06}_{-0.08}$	$12.86^{+0.17}_{-0.26}$
Model 3: WABS*PO+WABS*MEKAL$_s$+WABS*MEKAL$_h$								
0.72[e]	$2.17^{+0.09}_{-0.09}$	<0.54	$0.24^{+0.03}_{-0.04}$	$2.01^{+0.92}_{-0.74}$	$0.60^{+0.02}_{-0.02}$	392.7/340	$3.12^{+0.03}_{-0.16}$	$15.14^{+0.10}_{-0.62}$

Notes.
[a] Hydrogen absorption column in units of 10^{21} cm^{-2}, including the Galactic component (0.223×10^{21} cm^{-2}).
[b] Observed fluxes in the 0.3–10 keV band, in units of 10^{-13} erg s^{-1} cm^{-2}.
[c] Unabsorbed luminosities in the 0.3–10 keV band, in units of 10^{39} erg s^{-1} (assuming a distance of 16.3 Mpc).
[d] Same hydrogen column as applied to the power-law spectral component.
[e] Hydrogen column frozen. PO is the power-law continuum model and MEKAL is the thermal plasma model (solar abundances), where s = soft (lower temperature) component and h = hard (higher temperature) component. Model parameter errors correspond to 90% confidence limits for one parameter of interest. The best-fitting model is model 3 (highlighted in bold).

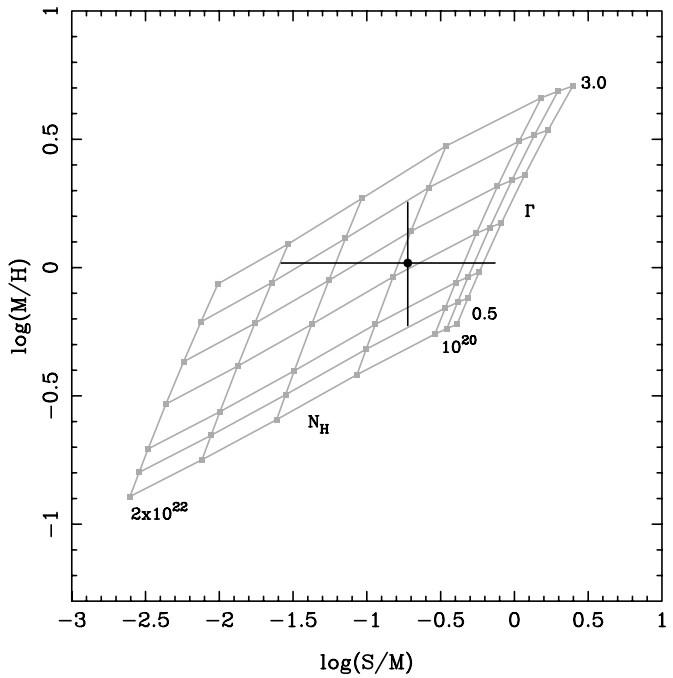

Figure 9. X-ray hardness ratio diagram for the nuclear source in NGC 1672 detected with *Chandra*, defined as the logarithm of the ratios of soft/medium and medium/hard band counts. The model grid, based on an ARF calculated on the position of the source, shows absorption values of $N_H = 10^{20}$, 5×10^{20}, 10^{21}, 5×10^{21}, 10^{22}, 1.5×10^{22}, and 2×10^{22} cm^{-2} (right to left), and photon indices of $\Gamma = 0.5$, 0.75, 1, 1.5, 2, 2.5, and 3 (bottom to top). The hardness ratios (and associated errors) were calculated using the BEHR algorithm (see the text for further details).

within the combined uncertainties. The 2–10 keV unabsorbed luminosity of the best-fit model is $2.70^{+0.10}_{-0.11} \times 10^{39}$ erg s^{-1}.

Note that there is no evidence for a bright AGN-like component that would be absorbed at low energies and only transmitted at higher energies. There is also no indication of a neutral Fe-6.4 keV emission line, typically seen in bright Type-2 AGN (although such a line, if present, would likely be diluted by the emission from the starburst ring). Inserting a narrow Gaussian line at 6.4 keV into the best-fit model, with all other model components frozen, results in a 90% upper limit on the equivalent width of ∼720 eV.

4.4.1. Long-term Variability

To search for spectral variability between the *XMM-Newton* and *Chandra* observations, we extracted an ACIS-S spectrum from the same nuclear region (Figure 10, bottom). This spectrum has significantly fewer counts than the *XMM-Newton* data (3070), therefore we froze the MEKAL temperatures and N_H values to those from the *XMM-Newton* best fit model, and only fit the power-law component. The slope is almost identical to the *XMM-Newton* observation with $\Gamma = 2.19^{+0.15}_{-0.16}$, and the model has a similar unabsorbed 2–10 keV luminosity of $2.50^{+0.37}_{-0.28} \times 10^{39}$ erg s^{-1}, which is consistent with the sum of the hard emission from the nucleus and point sources in the circumnuclear ring.

The 0.2–2 keV luminosity of the central source in the *ROSAT*/HRI observations (X-1) remained almost constant at 7.4–7.0 $\times$ 10^{39} erg s^{-1} between the 1992 and 1997 observations (de Naray et al. 2000). The equivalent 0.2–2 keV luminosity in both the *XMM-Newton* and *Chandra* data is 8.2 $\times 10^{39}$ erg s^{-1} (corrected for Galactic absorption); there is therefore no evidence for significant variability (in the soft band) over an ∼14 year period.

5. DISCUSSION

5.1. The Nature of the Nuclear Source

The nuclear X-ray source in NGC 1672 is observed to have a hard X-ray spectrum, with detections in the medium (1–2 keV) and hard (2–10 keV) bands only. However, the spectral slope is not well constrained with the hardness ratio ($\Gamma = 1.5^{+1.0}_{-0.8}$) due to the low number of counts. This, in conjunction with its low observed 2–10 keV luminosity ($L_X \sim 4 \times 10^{38}$ erg s^{-1}) means that the underlying nature of the emission is not obvious. Given its location, it could be an accreting LLAGN, but there are several other possibilities. For example, the emission may be produced by one, or a few, XRBs associated with star formation in the nuclear region. Or it could be a composite object with some of the emission coming from an LLAGN and some from star formation. It may also be produced by compact supernovae (SNe)/supernova remnants (SNRs), also directly related to any star formation in the region. We investigate these possibilities as follows.

Garcia-Rissmann et al. (2005) have measured a stellar velocity dispersion of ∼110 km s^{-1} from the calcium triplet (λλ8498,

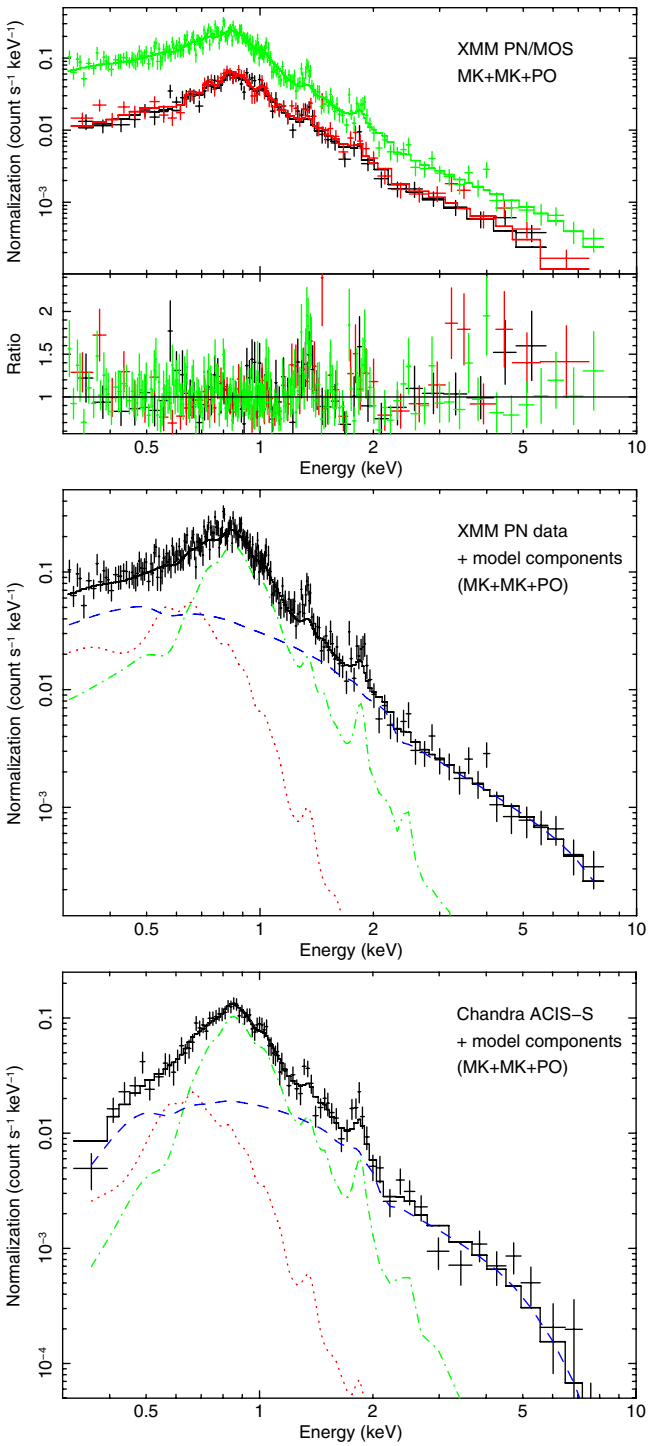

Figure 10. X-ray spectra from the central 22″ radius region of NGC 1672, which includes the nucleus and circumnuclear ring. Top: *XMM-Newton* folded model and PN (green) and MOS1/MOS2 (black/red) spectra. Middle: folded model and PN spectrum to illustrate the contributions from the model components, denoted by dashed blue (power law), dotted red (cool MEKAL), and dot-dashed green (warm MEKAL) lines. Bottom: the ACIS-S spectrum with MK+MK+PO model.

(A color version of this figure is available in the online journal.)

8542, 8662) lines in the inner 300 pc radius of NGC 1672. According to recent simulations and observational results (Younger et al. 2008; Hu 2008), the $M_{\rm BH}$–$\sigma_\star$ relation for supermassive black holes in galaxies with pseudobulges (such as NGC 1672, Fisher & Drory 2010) has a similar slope but lower normalization than that for galaxies with classical early-type bulges (see Figure 4 in Hu 2008). This new relation predicts a central black hole mass of only $\sim 10^6\ M_\odot$ for NGC 1672. If the central X-ray source is an LLAGN, then its luminosity implies a very low accretion rate, with $L_X/L_{\rm Edd} \sim 3\times10^{-6}$ (or $L_{\rm bol}/L_{\rm Edd} \sim 5\times10^{-5}$ if a bolometric correction for an LLAGN of $L_{\rm bol} = 15.8\,L_X$ for the 2–10 keV band is assumed; Ho 2009).

However, strong evidence of LLAGN activity comes from the radio imaging data, which shows that NGC 1672 has a compact 5 GHz radio core coincident with both the X-ray and optical nucleus (Figure 8(c)). Bright radio cores are frequently found in LLAGNs (e.g., Heckman 1980; Nagar et al. 2000) and are believed to be the signature of radio jets produced by accreting supermassive black holes with radiatively inefficient accretion flows. The flux densities of the radio source are 0.95 mJy ($\nu L_\nu = 2.6\times10^{36}$ erg s^{-1}) at 10 GHz (3 cm), and 1.62 mJy ($\nu L_\nu = 2.5\times10^{36}$ erg s^{-1}) at 5 GHz (6 cm); these translate into a steep spectral slope of $\alpha = -0.91 \pm 0.4$ (where $S_\nu \propto \nu^\alpha$). Both bright and low-level AGNs tend to have flat radio slopes ($\alpha \sim 0$), thought to result from self-absorption of synchrotron radiation from the base of a jet (Nagar et al. 2000), although flat slopes can also be produced by thermal emission from optically thin ionized gas in nuclear starbursts (Condon et al. 1991). However, steeper slopes ($-0.7 \lesssim \alpha \lesssim -0.2$) can be explained by optically thin synchrotron emission from jets on larger scales (Nagar et al. 2001), which is consistent with our result. SNRs are also expected to produce steep radio slopes ($-0.7 \lesssim \alpha \lesssim -0.4$), and we investigate this possibility below. In contrast, radio emission from an advection-dominated accretion flow (Narayan & Yi 1995) is predicted to have an inverted radio spectrum ($0.2 \lesssim \alpha \lesssim 1.3$; Nagar et al. 2001), which is not consistent with our result.

To investigate whether the radio/X-ray properties of this source are consistent with a supermassive or stellar-mass black hole (i.e., a normal XRB), we can use the fundamental-plane relation of Merloni et al. (2003). This relation shows that the 5 GHz radio luminosity, 2–10 keV X-ray luminosity, and black hole mass are strongly correlated for both Galactic (stellar-mass) black holes and central supermassive black holes for a range of accretion rates, which is believed to result from an intimate connection between accretion flow and jet activity. The radio luminosity of the nuclear source in NGC 1672 is fully consistent with that expected from a jet from a $\sim 10^6\ M_\odot$ supermassive black hole (in combination with $L_{\rm X} = 4\times10^{38}$ erg s^{-1}), and approximately five orders of magnitude too luminous for a jet from a typical 10 $M_\odot$ stellar-mass black hole (see their Figure 5). This effectively rules out the normal XRB scenario. (Note that a similar result is found for the one off-nuclear X-ray source with a radio counterpart; see Section 4.1.)

We can also estimate the probability of a chance coincidence of an XRB with the nucleus, using the "Universal" luminosity functions of high-mass XRBs (HMXBs; Grimm et al. 2003) and low-mass XRBs (LMXBs; Gilfanov 2004), which depend on star formation rate and stellar mass, respectively. To calculate the SFR for the nuclear region only (excluding contributions from the ring), we use a spatially resolved, Hα line flux measured in the central 2″ of the galaxy (9.2×10^{38} erg s^{-1}; Storchi-Bergmann et al. 1996) together with the Hα–SFR calibration of Kennicutt (1998, hereafter K98). A color excess of $E(B-V) = 0.16$ was derived from the Balmer decrement in the nuclear region, and the Hα flux is corrected for this. Note that we do not use the narrowband ACS Hα data for this purpose, since this filter ($F658N$) is known to be contaminated by the [N II] $\lambda\lambda$6583

and 6548 lines (O'Dell 2004). Using the K98 SFR calibration

$$\mathrm{SFR}(M_\odot\ \mathrm{yr}^{-1}) = \frac{L(\mathrm{H}\alpha)}{1.26\times10^{41}\ \mathrm{erg\ s}^{-1}}, \quad (1)$$

the Hα luminosity is equivalent to a nuclear SFR of 0.007 $M_\odot$ yr^{-1} (if star formation is the source of the emission). According to the relation of Grimm et al. (2003), this predicts only ~0.01 HMXBs with luminosities greater than 4×10^{38} erg s^{-1}. To estimate the stellar mass in the nuclear region, we use the *Spitzer*/IRAC 3.6 μm measurement as a proxy for the *K*-band luminosity, and convert this to stellar mass using the *K*-band mass-to-light ratio of Bell et al. (2003, $M_\star/L_K \sim 0.8\times M_\odot/L_{K,\odot}$), resulting in $M_\star \sim 4.2\times10^8 M_\odot$. The universal LMXB luminosity function (Gilfanov 2004) predicts only ~0.008 LMXBs above 4×10^{38} erg s^{-1} for this stellar mass.

The other possibility is that the X-ray and radio core emission arises from SNe/SNRs. Although soft thermal X-ray emission is the characteristic signature of SNe/SNRs (resulting from shock fronts interacting with circumstellar and ISM material, e.g., Immler & Lewin 2003), hard non-thermal emission is detected in some SNe, possibly emitted from a young pulsar left behind in a core-collapse event. An example of this is SN 1968D (Soria & Perna 2008), where the 2–10 keV component has $L_X \sim 10^{37}$ erg s^{-1}. However, the soft component dominates the 0.3–10 keV luminosity, with the hard emission only contributing ~10% to the total. This is not the case here; after careful background subtraction using the area inside the ring, there are no soft 0.3–1 keV counts. While this is likely due to absorption, the hard 2–10 keV band luminosity dominates the detected emission.

We can also use the radio data to investigate the SN/SNR option. Kewley et al. (2000) have previously detected compact radio emission at 2.3 GHz in the core of NGC 1672, and speculated, by calculating the theoretical radio SNR luminosity and comparing it to the observed luminosity, that it is possible that this can be produced by clumps of luminous radio SN, similar to those found in the nuclei of Arp 220 (Smith et al. 1998) and M82 (Huang et al. 1994). However, they used an SFR (derived from far-IR data) for the *whole* galaxy rather than the nuclear region, and therefore this was not conclusive evidence for or against the presence of an AGN. What is required is a similar test for the nuclear region only.

Following the recipe of Kewley et al. (2000), we take the SFR and calculate the expected supernova rate, ν_{SN}, integrating the SFR over a Salpeter initial mass function (IMF) with lower and upper mass limits of 0.1 $M_\odot$ and 100 $M_\odot$, and a minimum initial mass for supernova detonation, $m_{\mathrm{SN}} = 8\ M_\odot$:

$$\nu_{\mathrm{SN}} = \int_{m_{\mathrm{SN}}}^{m_u}\psi(m)dm \approx \frac{0.35\dot{m}}{1.35}\frac{\left(m_{\mathrm{SN}}^{-1.35} - m_u^{-1.35}\right)}{\left(m_l^{-0.35} - m_u^{-0.35}\right)}, \quad (2)$$

where $\dot{m}$ is the SFR. This results in $\nu_{\mathrm{SN}} = 5\times10^{-5}$ yr^{-1}. We can then calculate the non-thermal radio luminosity expected for this SN rate for both young SNe ($L_{\mathrm{NT}}^{\mathrm{YSN}}(\nu)$, with radio lifetime $t_{\mathrm{radio}} = 10$ yr), and old SNRs ($L_{\mathrm{NT}}^{\mathrm{SNR}}(\nu)$, with $t_{\mathrm{radio}} = 2\times10^4$ yr), using the following equations derived by Colina & Perez-Olea (1992) from observations of SN1979C:

$$L_{\mathrm{NT}}^{\mathrm{YSN}}(\nu) = 1.58\times10^{28}\left(\frac{\nu}{8.44\ \mathrm{GHz}}\right)^{-0.74}\nu_{\mathrm{SN}}\ \mathrm{erg\ s}^{-1}\ \mathrm{Hz}^{-1}, \quad (3)$$

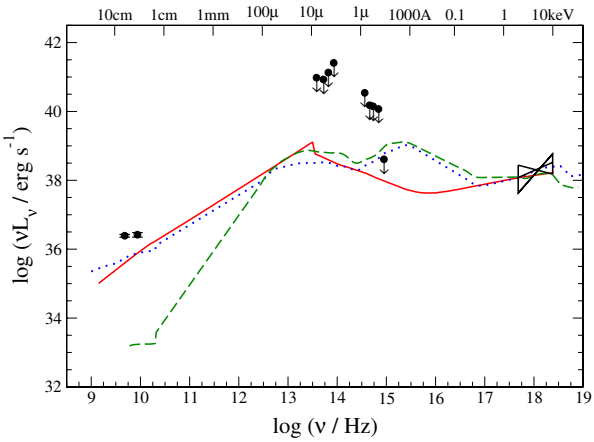

Figure 11. SED of the nuclear source in NGC 1672. The IR and optical measurements are shown as upper limits, since there is likely to be contamination from starlight at these wavelengths. Also plotted is the average LLAGN SED of Ho (2005) (solid red line), and the average radio-loud (dotted blue line) and radio-quiet (dashed green line) quasar SEDs of Elvis et al. (1994), normalized to the X-ray luminosity of NGC 1672 at 2 keV.

(A color version of this figure is available in the online journal.)

$$L_{\mathrm{NT}}^{\mathrm{SNR}}(\nu) = 1.77\times10^{29}\left(\frac{\nu}{8.44\ \mathrm{GHz}}\right)^{-0.74}\nu_{\mathrm{SN}}\ \mathrm{erg\ s}^{-1}\ \mathrm{Hz}^{-1}. \quad (4)$$

For the nuclear source in NGC 1672, these predict $\nu L_{\mathrm{NT}}^{\mathrm{YSN}}(\nu) = 6.1\times10^{33}$ erg s^{-1} and $\nu L_{\mathrm{NT}}^{\mathrm{SNR}}(\nu) = 6.8\times10^{34}$ erg s^{-1} at 5 GHz. The total of the two is a factor of 34 lower than the measured luminosity of the compact central source at this frequency ($\nu L_\nu = 2.5\times10^{36}$ erg s^{-1}), which indicates that SNRs are not the primary source of the radio emission. However, we must consider the uncertainties associated with the SFR conversion and extinction correction used here. Kennicutt et al. (2009) have made a detailed investigation of the systematic uncertainties associated with the Balmer decrement correction, and find it to be accurate to 15% on average. Indeed, apart from variations in the IMF, the amount of extinction present is the dominant source of uncertainty in the Hα–SFR conversion (Kennicutt et al. 2009). Once the correction has been applied, additional uncertainties arise from variations in metallicity and stellar ages, but only at the ~20% level (Calzetti et al. 2007). Taking these factors into consideration, we conclude that SNRs cannot easily account for the high radio output in the core of NGC 1672.

5.2. The Spectral Energy Distribution

Figure 11 shows the SED of the nuclear source, constructed using the spatially resolved measurements at radio, near-IR, optical, UV, and X-ray wavelengths. The X-ray spectral slope plus upper/lower limits estimated from the hardness ratio, are shown in νL_ν units as a "bow-tie." For comparison, we also plot the average LLAGN SED of Ho (2005), as well as the average SEDs of radio-quiet and radio-loud quasars from Elvis et al. (1994), which are all normalized to the 2 keV nuclear X-ray luminosity of NGC 1672.

These measurements allow us to derive some useful broad spectral properties of the source. One such diagnostic is its radio "loudness." Terashima & Wilson (2003) define a ratio of radio-to-X-ray luminosity, $R_{\mathrm{X}} = \nu L_\nu$ (5 GHz)/L_{X}, which is more sensitive to highly absorbed sources than the traditional radio-to-*B*-band luminosity ratio. A 5 GHz radio luminosity of $\nu L_\nu = 2.5\times10^{36}$ erg s^{-1} and a 2–10 keV X-ray luminosity of

$L_X = 4 \times 10^{38}$ erg s^{-1} gives log $R_X = -2.2$, which classifies the nucleus of NGC 1672 as radio loud (see their Figure 5). This is consistent with other LLAGNs and the hypothesis that the majority of LLAGNs possess relativistic jets (e.g., Ho 2005).

Given the scaling of the comparison SEDs, the radio luminosity of NGC 1672 is consistent with that of both the average LLAGN and radio-loud quasars. However, there is a clear excess of emission at near-IR and optical wavelengths with respect to the average SEDs, which indicates that the photometry is contaminated by star formation in the region. Indeed, the optical *HST* measurements are considered to be upper limits on the luminosity of a nuclear point source (Section 3.4.1), and we denote them, and the near-IR measurements, as such with arrows. This excess indicates that the nuclear emission is a combination of both a low-accretion-rate central black hole and star formation in the central ∼200 pc around the black hole; this agrees with the study of Veron et al. (1981), who detected both narrow and slightly broadened weak optical emission lines in the central $2'' \times 4''$ nuclear region (see Section 2) and concluded that they likely represent a composite H II/Seyfert nucleus.

We can also test whether the Hα luminosity is consistent with the $L_X/L_{H\alpha}$ correlation of Ho et al. (2001) for AGNs. The underlying physical reason for this relation, which holds from bright quasars all the way down to the LLAGN regime, is that the optical emission lines are powered by photoionization from a hard AGN continuum, which naturally scales with the X-ray luminosity. Type-1 objects follow the relation strongly, while Type-2 Seyferts/LLAGNs tend to be more underluminous in X-rays (see Figure 2 in Ho et al. 2001). This suggests that either the Hα luminosity may also have a contribution from other processes (e.g., star formation) in the vicinity of the central black hole in these objects, or that the AGN is highly absorbed and therefore only appears underluminous in the X-ray band (Terashima & Wilson 2003). The nuclear source of NGC 1672, with $L_X = 4 \times 10^{38}$ erg s^{-1} and $L_{H\alpha} = 9 \times 10^{38}$ erg s^{-1}, is underluminous in X-rays, consistent with other Type-2 AGNs in the Ho et al. (2001) survey. Flohic et al. (2006) show a similar figure for a sample of LINERs observed with *Chandra*, and also include luminosity ranges where a pure starburst would fall (see their Figure 7). The nuclear source in NGC 1672 falls in the region below the Ho et al. (2001) AGN relation and above that expected for starbursts, again strongly suggesting that this is a Type-2 AGN.

We have also calculated *Spitzer*/IRAC colors to compare with the color–color diagram of Sajina et al. (2005), which separates PAH-dominated (star-forming), stellar-dominated (passive), and continuum-dominated (AGN) sources. The colors of the nuclear source of NGC 1672 ($\log[f_\nu 5.8/f_\nu 3.6] = -0.27 \pm 0.03$ and $\log[f_\nu 8.0/f_\nu 4.5] = 0.10 \pm 0.01$) fall at the intersection of all three source types, indicating again that there is some star formation activity in the nuclear region (which agrees with the imaging, see Figure 8(d), where the PAH emission is clearly visible).

5.3. Is the Nucleus Compton-thick?

Since there is evidence for a composite nucleus with some absorption, we can investigate whether it is Compton-thick ($N_H > 10^{24}$ cm^{-2}). Observationally, the nuclear source is faint and hard at X-ray wavelengths, with an upper limit on the absorption of a modest value of $N_H \sim 1.5 \times 10^{22}$ cm^{-2} (as derived from the hardness ratio). However in Compton-thick sources, the direct X-ray emission is completely suppressed below ∼10 keV; the observed 2–10 keV component represents X-rays reflected or scattered by surrounding material, which tends to produce a hard X-ray spectrum (Bassani et al. 1999; Cappi et al. 2006). Therefore, the observed luminosity and spectral slope will not be representative of the intrinsic properties of the source (e.g., the archetypal Seyfert 2 galaxy NGC 1068; Matt et al. 1997; Iwasawa et al. 1997), and may lead to misclassification as a moderately absorbed LLAGN.

An X-ray signature of a Compton-thick AGN is a strong Fe Kα line at 6.4 keV (equivalent width typically $\gtrsim$1 keV), due it being measured against a depressed X-ray continuum (Bassani et al. 1999). However, in the case of NGC 1672 we cannot place any meaningful limits on the presence of such a line due to the low number of counts in the *Chandra* detection. The 720 eV equivalent width upper limit from the *XMM-Newton* spectral fits (see Section 4.4) does not provide a good constraint due to dilution by sources in the circumnuclear ring.

Other multiwavelength measurements can also provide evidence for the presence or absence of strong absorption. For example, an indicator that a source may be highly absorbed is the ratio of 2–10 keV X-ray flux to the [O III] λ5007 line flux. The [O III] line is believed to be a measure of the intrinsic brightness of the source since it is produced by the photoionizing AGN continuum, but in the narrow line region far from the nucleus (see Cappi et al. 2006, and references therein). Storchi-Bergmann et al. (1996) measured the [O III] flux from the central 2″ of NGC 1672 as $1.15 \pm 0.12 \times 10^{-14}$ erg s^{-1} cm^{-2}. Together with the observed 2–10 keV X-ray flux of $1.17^{+0.55}_{-0.39} \times 10^{-14}$ erg s^{-1} cm^{-2}, this gives $F_{2-10\ \mathrm{keV}}/F_{[\mathrm{O\,III}]} = 0.99^{+0.47}_{-0.34}$. Unfortunately, this is inconclusive, as it falls on the borderline of the Compton-thick category (typically <1, Bassani et al. 1999; Cappi et al. 2006), and some confirmed Compton-thick galaxies have ratios within our error range (e.g., NGC 3079; Cappi et al. 2006). However, it indicates that there is some absorption in the nucleus, which is consistent with Type-2 classification.

6. COMPARISON WITH OTHER NEARBY GALAXIES

How do the results for NGC 1672 fit into the broader picture of AGN evolution? Do more barred galaxies than non-barred galaxies contain AGNs because of the extra fuel provided, and what are their X-ray luminosities? What effect does the presence of a circumnuclear ring have?

A preliminary inspection of published results for nearby spiral galaxies observed with *Chandra* to date reveals a large range of observed nuclear X-ray properties, regardless of morphological type. For instance, while the strongly barred galaxies NGC 1365, NGC 1386, NGC 3079, and NGC 3393 are classified as Compton-thick, with absorption-corrected 2–10 keV X-ray luminosities of $>10^{42}$ erg s^{-1} (Risaliti et al. 2005; Levenson et al. 2006; Panessa et al. 2006), other strongly barred systems such as NGC 660, NGC 1023, and NGC 2787 (Dudik et al. 2005; Zhang et al. 2009) have observed nuclear luminosities of only 10^{38}–10^{39} erg s^{-1}. A similar range of X-ray luminosities is found for unbarred galaxies, such as M31 and M51 ($L_X \sim 10^{37}$ erg s^{-1}, $L_X \sim 10^{41}$ erg s^{-1}; Dudik et al. 2005), M33 ($L_X \sim 10^{38}$ erg s^{-1}; La Parola et al. 2003), and NGC 7212 ($L_X \sim 10^{43}$ erg s^{-1}; Levenson et al. 2006).

The range of nuclear luminosities for galaxies with circumnuclear rings, which are predominantly found in barred galaxies (e.g., Knapen 2005a), is also broad. Examples are NGC 4736 ($L_X \sim 10^{38}$ erg s^{-1}; González-Martín et al. 2006), NGC 4303 ($L_X \sim 10^{39}$ erg s^{-1}; Jiménez-Bailón et al. 2003), NGC 1097 ($L_X \sim 10^{40}$ erg s^{-1}; Nemmen et al. 2006), NGC 1365 ($L_X \sim$

10^{42} erg s^{-1}; Risaliti et al. 2005), and even non-detections in some cases such as NGC 3351 ($L_X \lesssim 10^{36}$ erg s^{-1}; Swartz et al. 2006) and NGC 4314 ($L_X \lesssim 10^{37}$ erg s^{-1}; Flohic et al. 2006). This indicates that the presence of a ring does not affect the X-ray luminosity of the nucleus in an obvious or straightforward way. For example, they do not all possess low-luminosity nuclei, which would be expected if a ring prevents the fuel from reaching the very center of the galaxy, a scenario suggested by Ho et al. (1997). It is also possible that galaxies with non- or low-luminosity detections have AGNs that are highly absorbed, or even Compton-thick, which is more likely in barred systems due to the increase in gas/star formation activity in the central regions.

In a recent survey of 187 nearby galaxies observed with *Chandra*, Zhang et al. (2009) found no correlation between the presence of a strong bar and the frequency or X-ray luminosity of nuclear sources. Indeed, they found a possible anti-correlation, in that strongly barred galaxies tend to have less-active nuclei than unbarred or weakly-barred galaxies. However, this study did not take into account the presence/absence of circumnuclear rings, or other smaller-scale features such as nuclear bars. Additionally, hydrodynamic mechanisms such as turbulence in the ISM close to the nucleus (e.g., nuclear spirals) may play a significant role in AGN fueling (Martini et al. 2003). Clearly, an extensive multiwavelength investigation is required to untangle the possible effects of large- and small-scale morphological features, as well as significant absorption on the X-ray properties of AGNs. That is beyond the scope of this paper, but will be addressed in a future study.

7. SUMMARY AND CONCLUSIONS

This paper is part of a continuing study in which we are aiming to ascertain how both the large- and small-scale morphology of a galaxy may affect its nuclear activity. We are studying this primarily from an X-ray perspective, as X-ray observations provide an ideal tool for searching for low-level nuclear activity that may not be visible at other wavelengths. Here we have performed a pilot study on the nearby barred spiral galaxy NGC 1672, using the high-spatial-resolution imaging power of *Chandra*, in conjunction with the spectral capabilities of *XMM-Newton*, to study the X-ray properties of the nuclear emission. We have supplemented this with multiwavelength imaging data from the *HST*/ACS, *Spitzer*/IRAC and ATCA ground-based radio observations. We have also analyzed the X-ray point source and diffuse emission properties of this galaxy. Our main results can be summarized as follows.

1. We detect 28 X-ray sources within the D_{25} area of the galaxy, ranging between $L_X = 7.4 \times 10^{37}$and 9.0×10^{39} erg s^{-1} in the 0.3–10 keV band. The positions of many of the sources outside the nuclear region correlate with star formation in the bar and spiral arms, and two are identified as background galaxies in the *HST* images. Nine of the X-ray sources are ULXs, with the three brightest ($L_X > 5 \times 10^{39}$ erg s^{-1}) located at the ends of the bar. There is also a diffuse component that traces star formation in the bar region, with a total X-ray luminosity of 9.0×10^{39} erg s^{-1} in the 0.5–2 keV band.
2. With high-spatial-resolution *Chandra* imaging, we have shown, for the first time, that NGC 1672 possesses a hard ($\Gamma \sim 1.5$) nuclear X-ray source, with a low 2–10 keV luminosity of 4×10^{38} erg s^{-1} (Figure 8). This in turn is surrounded by an X-ray-bright circumnuclear star-forming ring (comprised of point sources and hot gas), which dominates the 2–10 keV X-ray emission in the central region of the galaxy (2.7×10^{39} erg s^{-1} within a radius of 22″). The ring structure and nuclear source are also present in the radio and IR imaging. The central ring region is not spatially resolved with *XMM-Newton*, but spectral fits indicate that there is no significant long-term variability of the nuclear flux over the two-year period between the *XMM-Newton* and *Chandra* observations, or with respect to *ROSAT*/HRI observations 9 and 14 years earlier.
3. Spatially resolved, multiwavelength photometry of the nuclear source supports the hypothesis that it is an LLAGN accreting at a low rate ($L_X/L_{\rm Edd} \sim 3 \times 10^{-6}$). The main discriminator is a bright radio counterpart, which cannot be easily accounted for by other possibilities such as a normal XRB or the combined emission from young SNe/SNRs. The broadband SED is consistent with a radio-loud LLAGN, although an excess of optical and IR flux indicates the presence of star formation activity close to the central black hole. The *HST* imaging also shows the presence of a nuclear spiral, which is a candidate mechanism for AGN fueling (Martini et al. 2003). While the X-ray hardness ratio indicates that there is some absorption present in the nuclear region ($N_{\rm H} < 1.5 \times 10^{22}$ cm^{-2}), the ratio of the 2–10 keV X-ray flux to the [O III] λ5007 line flux does not provide strong evidence that the nucleus is Compton-thick.

A preliminary investigation of published results shows that both barred and unbarred spiral galaxies possess a broad range of observed nuclear X-ray luminosities. To further investigate the effect that bars and their associated circumnuclear features have on their nuclear activity, we are conducting a multiwavelength survey of nearby galaxies. Using optical/IR high-spatial-resolution imaging to resolve the circumnuclear structure in a well-matched sample of barred/unbarred galaxies, we will use complementary *Chandra* observations to measure their nuclear X-ray properties and search for a potentially absorbed AGN. Morphological classification of galaxies is also vitally important, as newer IR surveys (e.g., Laine et al. 2002) are discovering that more galaxies host bars than optical data suggest. Galaxies classed as "oval" should also be considered, since they may be just as effective as barred galaxies at moving gas from the disks of galaxies to their nuclear regions (Kormendy & Kennicutt 2004). These issues will be addressed in our ongoing study and will provide a crucial element in assessing the overall demography and evolution of supermassive black holes in the local universe.

We thank the referee for helpful comments that have improved the manuscript. L.P.J. acknowledges funding for the majority of this project from the NASA Postdoctoral Fellowship Program. W.N.B. acknowledges NASA ADP grant NNX10AC99G. This research has made use of software provided by the *Chandra* X-ray Center (CXC), which is operated by the Smithsonian Astrophysical Observatory for and on behalf of the National Aeronautics Space Administration under contract NAS8-03060. The *XMM-Newton* observatory is an ESA science mission with instruments and contributions directly funded by ESA Member States and NASA. Observations made with the NASA/ESA *Hubble Space Telescope* were obtained from the data archive at the Space Telescope Institute. STScI is operated by the association of Universities for Research in Astronomy, Inc. under the NASA contract NAS 5-26555. The *Spitzer*

Space Telescope is operated by the Jet Propulsion Laboratory, California Institute of Technology under a contract with NASA. The Australia Telescope Compact Array is part of the Australia Telescope which is funded by the Commonwealth of Australia for operation as a National Facility managed by CSIRO. This research has made use of the NASA/IPAC Infrared Science Archive, which is operated by the Jet Propulsion Laboratory, California Institute of Technology, under contract with NASA.

REFERENCES

Barlow, R. 2004, arXiv:physics/0406120
Bassani, L., Dadina, M., Maiolino, R., Salvati, M., Risaliti, G., della Ceca, R., Matt, G., & Zamorani, G. 1999, ApJS, 121, 473
Bauer, F. E., Alexander, D. M., Brandt, W. N., Schneider, D. P., Treister, E., Hornschemeier, A. E., & Garmire, G. P. 2004, AJ, 128, 2048
Bell, E. F., McIntosh, D. H., Katz, N., & Weinberg, M. D. 2003, ApJS, 149, 289
Böker, T., Sarzi, M., McLaughlin, D. E., van der Marel, R. P., Rix, H.-W., Ho, L. C., & Shields, J. C. 2004, AJ, 127, 105
Brandt, W. N., Halpern, J. P., & Iwasawa, K. 1996, MNRAS, 281, 687
Broos, P. S., Townsley, L. K., Feigelson, E. D., Getman, K. V., Bauer, F. E., & Garmire, G. P. 2010, ApJ, 714, 1582
Buta, R. 1999, Ap&SS, 269, 79
Buta, R., & Combes, F. 1996, Fundam. Cosm. Phys., 17, 95
Calzetti, D., et al. 2007, ApJ, 666, 870
Campana, S., Moretti, A., Lazzati, D., & Tagliaferri, G. 2001, ApJ, 560, L19
Cappi, M., et al. 2006, A&A, 446, 459
Cash, W. 1979, ApJ, 228, 939
Chen, L.-W., Fabian, A. C., & Gendreau, K. C. 1997, MNRAS, 285, 449
Colina, L., & Perez-Olea, D. 1992, MNRAS, 259, 709
Condon, J. J., Huang, Z.-P., Yin, Q. F., & Thuan, T. X. 1991, ApJ, 378, 65
De Luca, A., & Molendi, S. 2004, A&A, 419, 837
de Naray, P. J., Brandt, W. N., Halpern, J. P., & Iwasawa, K. 2000, AJ, 119, 612
Desroches, L.-B., & Ho, L. C. 2009, ApJ, 690, 267
de Vaucouleurs, G., de Vaucouleurs, A., Corwin, H. G. Jr., Buta, R. J., Paturel, G., & Fouque, P. 1991, Third Reference Catalog of Bright Galaxies (Vol. 1–3; Berlin: Springer)
Dudik, R. P., Satyapal, S., Gliozzi, M., & Sambruna, R. M. 2005, ApJ, 620, 113
Dudik, R. P., Satyapal, S., & Marcu, D. 2009, ApJ, 691, 1501
Elvis, M., et al. 1994, ApJS, 95, 1
Englmaier, P., & Gerhard, O. 1997, MNRAS, 287, 57
Eskridge, P. B., et al. 2000, AJ, 119, 536
Evans, I. N., Koratkar, A. P., Storchi-Bergmann, T., Kirkpatrick, H., Heckman, T. M., & Wilson, A. S. 1996, ApJS, 105, 93
Fazio, G. G., et al. 2004, ApJS, 154, 10
Fisher, D. B., & Drory, N. 2010, ApJ, 716, 942
Flohic, H. M. L. G., Eracleous, M., Chartas, G., Shields, J. C., & Moran, E. C. 2006, ApJ, 647, 140
Garcia-Rissmann, A., Vega, L. R., Asari, N. V., Cid Fernandes, R., Schmitt, H., González Delgado, R. M., & Storchi-Bergmann, T. 2005, MNRAS, 359, 765
Garcia-Vargas, M. L., Diaz, A. I., Terlevich, R. J., & Terlevich, E. 1990, Ap&SS, 171, 65
Giacconi, R., et al. 2001, ApJ, 551, 624
Gilfanov, M. 2004, MNRAS, 349, 146
González-Martín, O., Masegosa, J., Márquez, I., Guainazzi, M., & Jiménez-Bailón, E. 2009, A&A, 506, 1107
González-Martín, O., Masegosa, J., Márquez, I., Guerrero, M. A., & Dultzin-Hacyan, D. 2006, A&A, 460, 45
Goulding, A. D., & Alexander, D. M. 2009, MNRAS, 398, 1165
Grimm, H.-J., Gilfanov, M., & Sunyaev, R. 2003, MNRAS, 339, 793
Harnett, J. I. 1987, MNRAS, 227, 887
Heckman, T. M. 1980, A&A, 87, 152
Helou, G., et al. 2004, ApJS, 154, 253
Ho, L. C. 2005, Ap&SS, 300, 219
Ho, L. C. 2009, ApJ, 699, 626
Ho, L. C., Filippenko, A. V., & Sargent, W. L. W. 1997, ApJS, 112, 315
Ho, L. C., et al. 2001, ApJ, 549, L51
Hu, J. 2008, MNRAS, 386, 2242
Huang, Z. P., Thuan, T. X., Chevalier, R. A., Condon, J. J., & Yin, Q. F. 1994, ApJ, 424, 114
Immler, S., & Lewin, W. H. G. 2003, in Supernovae and Gamma-Ray Bursters, ed. K. Weiler (Lecture Notes in Physics, Vol. 598; New York: Springer), 91
Iwasawa, K., Fabian, A. C., & Matt, G. 1997, MNRAS, 289, 443
Jenkins, L. P., Roberts, T. P., Ward, M. J., & Zezas, A. 2005, MNRAS, 357, 109
Jiménez-Bailón, E., Santos-Lleó, M., Mas-Hesse, J. M., Guainazzi, M., Colina, L., Cerviño, M., & González Delgado, R. M. 2003, ApJ, 593, 127
Kennicutt, R. C., Jr. 1998, ApJ, 498, 541
Kennicutt, R. C., Jr., et al. 2009, ApJ, 703, 1672
Kewley, L. J., Heisler, C. A., Dopita, M. A., Sutherland, R., Norris, R. P., Reynolds, J., & Lumsden, S. 2000, ApJ, 530, 704
Knapen, J. H. 2005a, A&A, 429, 141
Knapen, J. H. 2005b, in AIP Conf. Proc. 783, The Evolution of Starbursts, ed. S. Hüttmeister et al. (Melville, NY: AIP), 171
Koekemoer, A. M., Fruchter, A. S., Hook, R. N., & Hack, W. 2002, in The 2002 HST Calibration Workshop: Hubble After the Installation of the ACS and the NICMOS Cooling System, ed. S. Arribas, A. Koekemoer, & B. Whitmore (Baltimore, MD: STScI), 337
Kormendy, J., & Kennicutt, R. C., Jr. 2004, ARA&A, 42, 603
Kuntz, K. D., & Snowden, S. L. 2001, ApJ, 554, 684
Kuntz, K. D., & Snowden, S. L. 2010, ApJS, 188, 46
Laine, S., Shlosman, I., Knapen, J. H., & Peletier, R. F. 2002, ApJ, 567, 97
La Parola, V., Damiani, F., Fabbiano, G., & Peres, G. 2003, ApJ, 583, 758
Levenson, N. A., Heckman, T. M., Krolik, J. H., Weaver, K. A., & Życki, P. T. 2006, ApJ, 648, 111
Lira, P., Ward, M., Zezas, A., Alonso-Herrero, A., & Ueno, S. 2002, MNRAS, 330, 259
Maiolino, R., Risaliti, G., & Salvati, M. 1999, A&A, 341, L35
Makovoz, D., Roby, T., Khan, I., & Booth, H. 2006, Proc. SPIE, 6274, 62740C
Martini, P., Regan, M. W., Mulchaey, J. S., & Pogge, R. W. 2003, ApJ, 589, 774
Mateos, S., et al. 2008, A&A, 492, 51
Matt, G., et al. 1997, A&A, 325, L13
Menéndez-Delmestre, K., Sheth, K., Schinnerer, E., Jarrett, T. H., & Scoville, N. Z. 2007, ApJ, 657, 790
Merloni, A., Heinz, S., & di Matteo, T. 2003, MNRAS, 345, 1057
Nagar, N. M., Falcke, H., & Wilson, A. S. 2005, A&A, 435, 521
Nagar, N. M., Falcke, H., Wilson, A. S., & Ho, L. C. 2000, ApJ, 542, 186
Nagar, N. M., Wilson, A. S., & Falcke, H. 2001, ApJ, 559, L87
Narayan, R., & Yi, I. 1995, ApJ, 452, 710
Nemmen, R. S., Storchi-Bergmann, T., Yuan, F., Eracleous, M., Terashima, Y., & Wilson, A. S. 2006, ApJ, 643, 652
O'Dell, C. R. 2004, PASP, 116, 729
Osmer, P. S., Smith, M. G., & Weedman, D. W. 1974, ApJ, 192, 279
Panessa, F., Bassani, L., Cappi, M., Dadina, M., Barcons, X., Carrera, F. J., Ho, L. C., & Iwasawa, K. 2006, A&A, 455, 173
Park, T., Kashyap, V. L., Siemiginowska, A., van Dyk, D. A., Zezas, A., Heinke, C., & Wargelin, B. J. 2006, ApJ, 652, 610
Risaliti, G., Elvis, M., Fabbiano, G., Baldi, A., & Zezas, A. 2005, ApJ, 623, L93
Sajina, A., Lacy, M., & Scott, D. 2005, ApJ, 621, 256
Satyapal, S., Dudik, R. P., O'Halloran, B., & Gliozzi, M. 2005, ApJ, 633, 86
Satyapal, S., Sambruna, R. M., & Dudik, R. P. 2004, A&A, 414, 825
Sérsic, J. L., & Pastoriza, M. 1965, PASP, 77, 287
Shlosman, I., Begelman, M. C., & Frank, J. 1990, Nature, 345, 679
Sirianni, M., et al. 2005, PASP, 117, 1049
Smith, H. E., Lonsdale, C. J., Lonsdale, C. J., & Diamond, P. J. 1998, ApJ, 493, L17
Snowden, S. L., et al. 1997, ApJ, 485, 125
Soria, R., & Perna, R. 2008, ApJ, 683, 767
Stobbart, A.-M., Roberts, T. P., & Wilms, J. 2006, MNRAS, 368, 397
Storchi-Bergmann, T., Kinney, A. L., & Challis, P. 1995, ApJS, 98, 103
Storchi-Bergmann, T., Wilson, A. S., & Baldwin, J. A. 1996, ApJ, 460, 252
Swartz, D. A., Yukita, M., Tennant, A. F., Soria, R., & Ghosh, K. K. 2006, ApJ, 647, 1030
Terashima, Y., & Wilson, A. S. 2003, ApJ, 583, 145
Veron, M. P., Veron, P., & Zuiderwijk, E. J. 1981, A&A, 98, 34
Wilms, J., Allen, A., & McCray, R. 2000, ApJ, 542, 914
Wright, A. E., Griffith, M. R., Burke, B. F., & Ekers, R. D. 1994, ApJS, 91, 111
Younger, J. D., Hopkins, P. F., Cox, T. J., & Hernquist, L. 2008, ApJ, 686, 815
Zhang, W. M., Soria, R., Zhang, S. N., Swartz, D. A., & Liu, J. F. 2009, ApJ, 699, 281